JOURNAL OF GEOPHYSICAL RESEARCH, VOL. 104, NO. A4, PAGES 6953–6971, APRIL 1, 1999

Electromagnetic ion cyclotron waves in the near-Earth magnetotail

C. C. Chaston[1], Y. D. Hu, and B. J. Fraser

Department of Physics, University of Newcastle, New South Wales, Australia

Abstract. This study considers the characteristics and generation mechanisms of bursts of polarized transverse electromagnetic waves observed over the frequency range from 50 up to 500 mHz in the near-Earth magnetotail from ISEE 1 and ISEE 2. Since this range contains the cyclotron frequencies of the ion components found in this region of space, we loosely term these bursts "electromagnetic ion cyclotron waves" (EMICs). Nearly all wave events fall in the frequency and wavelength ranges of 50 to 150 mHz and 1000 to 6700 km, respectively, with amplitudes of the order of 1 nT and may exhibit both left- and right-hand polarizations. These waves propagate at wavenormal angles, θ_k<45°, and exhibit wave amplitudes where the ratio of the amplitude parallel ($b_\parallel$) to the background magnetic field ($\mathbf{B}_0$) to that perpendicular ($b_\perp$) to $\mathbf{B}_0$ varies proportionally with θ_k, and this ratio is typically less than 0.5. ISEE1 LEPEDEA distribution function data indicate that the polarized bursts are often accompanied by anisotropic ion distributions and or significant field-aligned currents. It is demonstrated that a positive correlation between the wave properties predicted from linear Vlasov theory and the observed field fluctuations exists for most wave events considered when the plasma is modeled using both bi-Maxwellian and bi-Lorentzian functional forms. The occurrence of these wave bursts is commonly synchronous with the decreasing phase of large-scale surface waves permeating the magnetotail, thereby suggesting that these waves provide a means of energy dissipation for global processes.

1. Introduction

Recently, the presence of magnetic field fluctuations in the ULF range in the near-Earth magnetotail has become increasingly apparent [*Angelopoulos et al.*, 1989; *Chaston et al.*, 1994; *Bauer et al.*, 1995]. These fluctuations cover a broad spectrum and in general obey the power law $\sim f^{2-2.5}$ [*Russell and McPherron*, 1972]. Such fluctuations are significant in magnetotail dynamics since they provide a means of rapid energy transport and maybe an important means whereby energy from macro-scale processes, such as eigenmode tail oscillations, cascade to microscale resonant wave particle interactions in the collisionless plasma of the magnetosphere. In fact, it has been suggested that the particle heating provided by wave-particle interactions of the kind discussed in this paper may provide the necessary anomalous resistivity in the neutral sheet to trigger substorms [*Lui et al.*, 1993].

While the spectrum of these fluctuations is broad, this paper seeks only to explain the occurrence of bursty polarized ULF waves in the magnetotail in the vicinity of the ion cyclotron frequency in terms of the predictions of linear Vlasov theory applied to ion and electron distributions observed coincident with the wave bursts. In agreement with the work of *Angelopoulos et al.* [1989] the ion cyclotron anisotropy [*Kennel and Petschek*, 1966; *Davidson and Ogden*, 1975; *Cupermann*, 1981; *Gary and Schriver*, 1987] and kink-like instabilities [*Hasegawa*, 1975; *Gary et al.*, 1976] are found to provide wave growth over the observed frequency range for both left- and right-hand polarizations. These bursts are distinct from the background magnetic noise in that they exhibit high degrees of polarization or coherency between the transverse field components and spectral energy densities an order of magnitude above background levels.

This work makes a contribution to the understanding of wave emissions associated with nonthermal particle distributions in the magnetosphere. In particular, it emphasizes the direct dependence of the observed wave characteristics upon the nature of the particle distributions present at the wave source and in this way is an experimental test of linear Vlasov instability theory and its applicability to the turbulent plasma of the magnetotail.

In this study the general characteristics of the polarized wave events observed will be discussed. The results go beyond those presented by *Angelopoulos et al.* [1989] and *Chaston et al.* [1994] to consider wave observations from the outer edge of the plasma sheet boundary layer to the central plasma sheet with modeling based on fitted particle distributions assuming bi-Maxwellian and bi-Lorentzian form. Three representative case studies will be examined in detail. The observed magnetic field data are compared with modeled results based on the instabilities arising from the observed distribution functions. Finally, a discussion of the relevance of these observations to field fluctuations in the magnetotail in general is given to place them in context with the ubiquitous magnetic noise and the large-scale low-frequency waves present in the plasma sheet boundary layer and plasma sheet [*Cattell et al.*, 1986; *Bauer et al.*, 1995; *Russell and McPherron*, 1972].

The wave and particle data presented here were recorded by the UCLA fluxgate magnetometers [*Russell*, 1978] onboard ISEE 1 and 2, the Los Alamos Fast Plasma Experiment (FPE) on board ISEE 2 [*Bame et al.*, 1978], and the University of Iowa Low Energy Plasma Experiment (LEPEDEA) onboard ISEE 1 [*Frank et al.*, 1978].

[1]Now at Space Sciences Laboratory, University of California at Berkeley.

Paper number 1998JA900139.
0148-0227/99/1998JA900139$09.00

2. Wave Characteristics

Each wave event considered has been identified from ISEE fluxgate magnetometer observations and FPE microfiche plots from orbits 56-80 over the months April and May 1978 at those times when the spacecraft was located at X_{GSM} <-10 R_E. It was required that the field observations exhibited wave power above background levels at frequencies satisfying $\Omega_O^+ \leq \omega < \Omega_p$, where ω is the wave angular frequency observed in the spacecraft frame and Ω_p the proton cyclotron frequency. Further, it was required that these waves occurred in the presence of energetic particle fluxes characteristic of the plasma sheet or its boundary layer or inner edge of the magnetotail lobes.

The wave properties presented in Table 1 have been determined using both time and frequency domain techniques applied to the field components presented in a field-aligned coordinate system. Wavenormal directions, θ_k ($\tan\theta_k = k_\perp/k_\parallel$, where $\mathbf{k}$ is the wavevector and $\perp$ and $\parallel$ indicate directions perpendicular and parallel to the background magnetic field $\mathbf{B_0}$ respectively), and ellipticities have been determined from minimum variance analysis of the covariance matrix [*Means*, 1972] calculated over a 30-50 mHz band-width centered on the frequency of maximum wavepower for each burst. These results have then been checked against those determined from the Hermitian properties of the Fourier transform of the covariance matrix calculated over the complete range of frequencies up to the Nyquist frequency (500 mHz at 1-Hz sampling) using the time series analysis code "POLFILT" developed by *Samson and Olson* [1981]. This code provides a measure of the coherency between time series channels labeled the "degree of polarization." For coherent activity between channels it is required that the degree of polarization exceeds 70%. This measure of coherency, applied to the two field components transverse to the ambient field, is implemented as the final constraint upon polarized wave bursts to be included in this study.

From this analysis a total of 27 wave events with degrees of polarization exceeding 70% have been identified from a selection of ISEE 1/2 plasma sheet/plasma sheet boundary layer traversals over the orbits indicated above. The spatial distribution of these observations in the near-Earth magnetotail is illustrated using the GSM coordinate system in Figure 1. It should be noted that for the spacecraft intervals considered Z_{gsm} is always positive so that the field-aligned direction in this region of space is roughly earthward along X_{gsm}. The majority of wave events occur in the plasma sheet boundary layer with a few in the plasma sheet and magnetotail lobes identified from the ISEE LEPEDEA and FPE ion distribution functions observed at the time of wave observation.

The wave properties are presented graphically in Figure 2. The event duration varied from 3 to 10 min and is independent of wave frequency, proton cyclotron frequency, Ω_p and location. Figure 2a illustrates the variation of wave frequency with θ_k and indicates that nearly all the wave observations occur in a band from 50 to 150 mHz ($<\Omega_p$) with $\theta_k<45°$, and for most events $\theta_k<25°$. These properties suggest the operation of cyclotron resonant interaction between waves and particles leading to the observed transverse wave activity. Therefore theoretical study based upon the assumption of field-aligned wave propagation is justified. Furthermore, Figure 2b illustrates that the majority of wave events observed in the spacecraft frame have negative ellipticity or, assuming field-aligned propagation, left-handed polarization.

While the wave electric field vector, $\mathbf{E}_1$, appears to rotate in a left-handed sense the modulus of the ellipticity is typically less than 0.6. This is perhaps indicative of the effects of off field propagation ($\theta_k \neq 0$) [*Anderson et al.*, 1996] or the presence of a transverse finite background electric field [*Hu and Fraser*, 1992; *Dowdell et al.*, 1995]. In this regard, Figure 2c illustrates the relationship between θ_k and the ratio of the wave amplitude parallel ($b_\parallel$) to $\mathbf{B_0}$ to the transverse wave amplitude ($b_\perp$). A clear correlation is apparent, verifying the presence of a plane wave and implying that the majority of the compressional amplitude may be explained through oblique propagation. In addition, Figure 2d indicates the variation of the ratio $b_\parallel/b_\perp$ with $b_\perp$. The trendline here indicates a rise in compressional amplitude with transverse amplitude, suggesting that the compressional component is not representative of an independent mode but is in fact the field-aligned component of the plane wave which is propagating slightly off the field. The maximum transverse amplitude for each event is < 3 nT and mostly ≤1 nT with the compressional component typically less than 50% of this value. In general, the right-hand wave events have a larger compressional component.

The wavelengths quoted in Table 1 have been obtained by determining the phase difference between the wave observations from ISEE 1 and ISEE 2. Using the coordinates of each spacecraft, the relative phase enables a rough determination of the wavelength and direction of propagation to an accuracy limited by the sampling interval of the field data and the angular position of the second spacecraft with respect to the solid angle defined by the wavenormal vector and the background field direction. In cases where the spacecraft is separated by distances less than 100 km (close to apogee) the phase difference may be less than the angular separation between sample points (at that frequency). In such cases the accuracy of the wavelength determination is poor and in Table 1 is indicated as greater than the wavelength defined by the angular separation between data points.

Figure 3a illustrates the variation of the wave amplitude with the Auroral Electrojet (*AE*) index. For transverse wave amplitudes a positive correlation is apparent indicating that wave intensity increases with increasing *AE*, consistent with the broadband observations reported by *Bauer et al.* [1995]. Similarly, although not presented graphically here, $b_\parallel/b_\perp$ also increases slightly with *AE*. Significantly, the majority of wave events occurred when *AE* was less than 600 nT. Above this level the field variations became noisy and the plasma turbulent making the identification of individual wave modes difficult and the linear growth of such modes unlikely. The apparent dependence of wave amplitude on *AE* is indicative of the dependence of the wave properties on the energy density of the plasma. This association between observed wave properties and plasma characteristics is also evident from the correlation between increasing normalized frequency and increasing local plasma density as illustrated in Figure 3b. These results indicate the dependence of the frequency of the growing wave upon the moments of the distribution function and magnetic field strength suggesting that the majority of wave events considered are observed in the vicinity of the wave source.

3. Wave Event Modeling

Here an attempt is made to identify the local electromagnetic instability, if any, associated with each of the observed wave events considered. This is based on the predictions of the linear Vlasov theory with $\mathbf{k}\times\mathbf{B_0}=0$ applied to the observed particle distributions where available. The results of the modeling are summarized in Table 1. In each case, modeling is performed assuming both bi-Maxwellian and bi-Lorentzian (Kappa) [*Summers and Thorne*, 1992] distribution function profiles. This comparative study of instability associated with the two different functional

Table 1. Wave Properties of the Events Used in This Study

Date, 1978	Time UT	ISEE1 Coordinate	Location	Band, mHz	Ellipse	θ_k	$b_\perp$	$b_\parallel/b_\perp$	λ,km	B_0,nT	*AE*	Instability	Agreement	Unstable Component
8/3	1130-1135	-17.47, -3.65, 6.77	PS	90-120	-0.4	40.2	1	0.5	+6400	17.1	62	K	y	e-drift
13/3	1410-1416	-20.1, -5.63, 7.04	PSBL	110-130	-0.6	13.2	0.4	0.25	>-2600	23.9	300	N	n	
13/3	1430-1435	-20.15, -5.84, 6.94	PSBL	110-130	0.25	23.4	0.4	0.25	>-2600	23.9	300	A	n	anisotropic beam
15/3	1627-1632	-18.01, -3.27, 6.75	PSBL	60-90	-0.33	1.6	0.6	0.125	-4300	32.4	171	K	y	ion drift
15/3	1724-1732	-18.46, -3.99, 6.58	PSBL	40-70	-0.4	32.2	1	0.2	>+2700	33.6	114	A	y	anisotropic beam
16/3	0450-0456	-20.61, -7.08, 6.09	LOBE	80-110	0.25	15.2	0.9	0.5	>-2100	25.4	596	N	n	
18/3	1212-1217	-20.71, -4.48, 7.59	LOBE	60-90	0.57	6.1	0.5	0.2	>-3100	27.6	731	K	n	e-drift
22/3	1412-1417	-13.70, 1.48, 6.57	PS	80-110	0.5	6.3	0.6	0.333	-2300	38.5	252	K	y	e-drift
22/3	1418-1423	-13.70, 1.48, 6.57	PS	60-90	-0.57	66	0.6	0.666	+4700	39.5	252	A	y	anisotropic beam
27/3	0801-0805	-12.38, 2.93, 6.48	PSBL	45-65	0.2	31.9	1.75	0.57	6600	62.1	564	K	n	e-drift
27/3	0806-0813	-12.54, 2.93, 6.51	PSBL	170-190,80-120	-0.5	13.5	0.7	0.14	+6000	58.0	564	K	y	e-drift
1/4	1046-1052	-17.84, 2.86, 8.26	PSBL	60-90	-0.5	7.2	0.7	0.57	+6700	21.6	129			
2/4	1339-1348	-17.46, -3.75, 5.25	PS	60-80	-0.6	27	0.8	0.5	+5000	18.1	215			
2/4	1849-1852	-13.72, -5.19, 2.10	PS	200-250, 40-70	-0.8	18.7	1.3	0.38	>+4000	6.1	338	A	y	anisotropic ions
3/4	1050-1100	-10.58, 4.79, 6.14	PSBL	70-90	-0.25	37.8	1	0.4	>-4200	59.1	475	A	y	anisotropic beam

Table 1. (continued)

Date, 1978	Time UT	ISEE1 Coordinate	Location	Band, mHz	Ellipse	θ_k	$b_\perp$	$b_\parallel/b_\perp$	λ,km	B_0,nT	*AE*	Instability	Agreement	Unstable Component
14/4	1904-1908	-12.88, -2.87, 2.58	PS	30-60	-0.88	88	1.15	2.6	-	10.3	529	A+K	y	anisotropic ions+e-drift
15/4	1315-1321	-12.5, 6.96, 7.93	PSBL	50-70	0.67	10.4	0.5	0.2	-5800	36.7	395	K	n	e-drift
18/4	0731-0736	-17.53, 6.96, 9.57	PS	80-110	0.22	6.9	0.5	0.2		30.3	118	A	n	anisotropic beam
18/4	0920-0925	-18.21, 7.20, 9.29	PSBL	60-90	-0.5	36.0	1.1	0.45	-	26.7	105	A	y	anisotropic beam
23/4	1027-1034	-19.11, 7.83, 9.14	PSBL	90-120	-0.3	70	0.3	1	>-1000	19.8	272	K	y	e-drift
24/4	1115-1120	-9.94, -0.93, 2.12	PS	40-60	0.67	57.9	0.65	1	>-1704	23.0	672			
26/4	1242-1247	-16.46, 3.03, 5.76	PSBL	120-140	-0.4	16.0	0.6	0.17	>+1000	-	327	A	y	anisotropic ions
27/4	2005-2009	-15.46, 6.37, 12.32	PSBL	50-70	0.23	38.9	0.75	0.4	>+2400	26.9	269	A+K	y	anisotropic beam+e-drift
30/4	1001-1005	-16.83, 10.94, 9.19	LOBE	370-470	-0.67	53	3	1	>-1000	30.7	1055			
30/4	1021-1025	-16.94, 10.92, 9.17	LOBE	40-70	-0.33	45.8	2.75	0.55	-	47.1	1055	N	n	
30/4	1238-1242	-17.56, 10.38, 5.93	LOBE	100-120	-0.9	10.9	1	0.2	>+1000	57.2	984			
30/4	1322-1324	-17.73, 10.02, 9.60	LOBE	420-470	-0.4	0.5	0.6	0.17	-	49.6	899			

The ISEE 1 spacecraft GSM coordinates are those of the spacecraft within ±5 min of the middle of each wave event. The ellipticities are determined from the polarization hodogram between the X-Y components in the field-aligned system. Negative and positive ellipticities indicate left-hand and right-hand polarization, respectively. The transverse wave amplitude ($b_\perp$) is the maximum amplitude in the X or Y components. The > sign in the wavelength column indicates that the phase difference between ISEE 1 and ISEE 2 was less than the phase represented by 1 sample period (1 Hz) and consequently the wavelength may be larger than quoted. The sign of the wavelength indicates the direction of propagation. Positive (negative) wavelengths indicate propagation towards (away from) the Earth along (against) the field direction. *AE* values are hourly averages from the WDC-C2 for Geomagnetism at Kyoto University. Dash indicates a data gap. The last three columns present the results from the application of linear Vlasov theory to the distribution functions measured onboard ISEE 1 by the LEPEDEA experiment for each event considered. In cases where more than one instability is found, the instability given is that of the dominant growing wave mode providing growth over the observed frequency range. The anisotropy instability is indicated by "A" and the kink-like instability by "K." If the plasma is stable, an "N" appears. If the plasma is stable to electromagnetic fluctuations over the frequency range of the observed polarized wave event, then a "n" appears in the next column. This also applies if the observed and predicted polarization do not agree. In those cases where the distribution function data are not available the corresponding row is left blank.

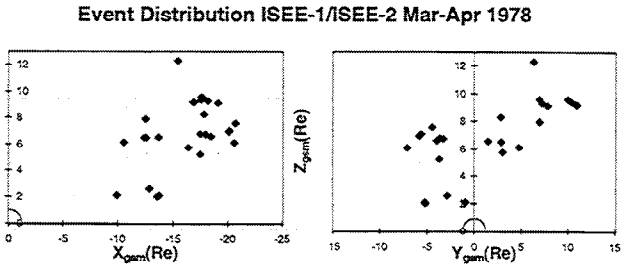

Figure 1. The spatial distribution of observed wave events in GSM coordinates measured in units of Earth radii (R_E).

forms is motivated by the studies of *DeCoster and Frank* [1979] and *Christon et al.* [1991], which indicate that ion distributions in the near-Earth magnetotail exhibit Maxwellian form below the thermal energy and extended tails with power law form above this energy. In general, these distributions most closely fit bi-Lorentzian profiles. Here we evaluate the significance of the different functional forms on instability identification.

The total ion density determined from each distribution function is assumed to be comprised of protons only and the plasma is taken to be charge neutral with the following definitions for each component (j): n_j is the number density, m_j is the particle mass, e_j is the particle charge, v_{0j} is the component drift velocity, $T_{\perp j}$ and $T_{\parallel j}$ are the temperatures in the directions perpendicular and parallel to $\mathbf{B_o}$ respectively, $\beta_j=8\pi n_j T_{\perp j}/B_o^2$ is plasma beta, $v_{Aj}=B_o/(4\pi n_j m_j)^{1/2}$ is the Alfven speed, $\Omega_j=q_jB_o/m_j$ is the cyclotron frequency, $\omega_j=(4\pi n_j q_j 2/m_j)^{1/2}$ is the plasma frequency, $v_j=(2T_{\parallel j}/m_j)^{1/2}$ is the thermal velocity and $a_j=v_j/|\Omega_j|$ is the Larmor radius.

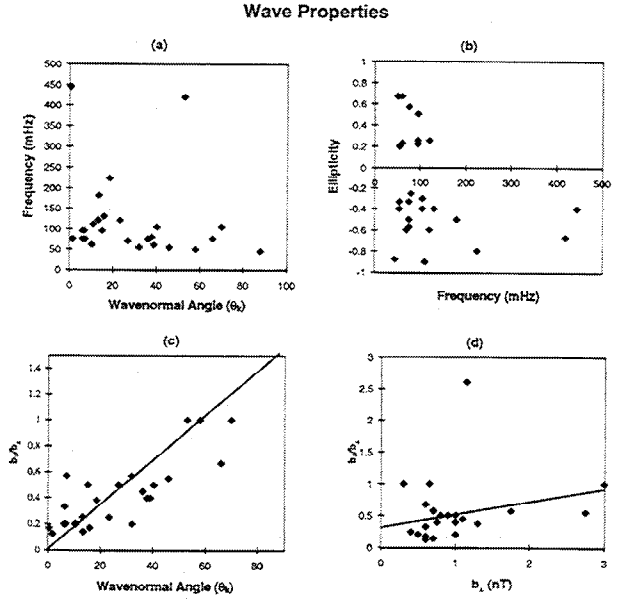

Figure 2. (a) The variation of wave frequency (at maximum power spectral density) with wavenormal angle, θ_k, determined from minimum variance analysis. (b) The variation of wave ellipticity with frequency. Here it is assumed that $\theta_k \approx 0°$ so negative and positive ellipticity indicate left-hand and right hand polarization respectively. (c) The variation in the ratio of compressional ($b_\parallel$) to transverse ($b_\perp$) wave amplitude with wavenormal angle. Amplitudes here represent the maximum amplitude in each component for each event. (d) The variation in the ratio of compressional to transverse wave amplitude with transverse wave amplitude.

The validity of the assumptions $\mathbf{k}\times\mathbf{B_o}=0$ and $n_H=n_{total}$ (i.e., no heavy ions) for the plasmas studied is justified in the appendix to this paper.

Solution of the linear Vlasov equation with $\mathbf{k}\times\mathbf{B_o}=0$ yields the well-known result,

$$\omega^2 - k_\parallel^2 c^2 + k_\parallel^2 c^2 \sum_j S_j^{\pm}(k_\parallel, \omega) = 0, \tag{1}$$

where the conductivity tensor $S_j^{\pm}$ for bi-Maxwellian components is [*Gary and Schriver*, 1987],

$$S_j^{\pm}(k_\parallel, \omega) = \frac{\omega_j^2}{k_\parallel^2 c^2}\left[\frac{\omega - k_\parallel v_{0j}}{k_\parallel v_j} Z(\xi_j^{\pm}) - \left(1 - \frac{T_{\perp j}}{T_{\parallel j}}\right)(1 + \xi_j^{\pm} Z(\xi_j^{\pm}))\right], \tag{2}$$

and for bi-Lorentzian components [*Summers and Thorne*, 1992; *Mace and Hellberg*, 1995; *Chaston et al.*, 1997],

$$S_j^{\pm}(k_\parallel, \omega) = \frac{\omega_j^2}{k_\parallel^2 c^2}\left[\frac{\omega - k_\parallel v_{0j}}{k_\parallel v_{\kappa j}}\left(\frac{\kappa_j}{\kappa_j - \frac{3}{2}}\right)\left(\frac{\kappa_j - 1}{\kappa_j}\right)^{\frac{3}{2}} Z_{\kappa_j - 1}\left(\sqrt{\frac{\kappa_j - 1}{\kappa_j}}\xi_j^{\pm}\right) - \left(1 - \frac{T_{\perp j}}{T_{\parallel j}}\right)\left(1 + \left(\frac{\kappa_j - 1}{\kappa_j - \frac{3}{2}}\right)\sqrt{\frac{\kappa_j - 1}{\kappa_j}}\xi_j^{\pm} Z_{\kappa_j - 1}\left(\sqrt{\frac{\kappa_j - 1}{\kappa_j}}\xi_j^{\pm}\right)\right)\right], \tag{3}$$

Here $Z(\xi_j^{\pm})$ and $Z_{\kappa j-1}(\xi_j^{\pm})$ are the plasma dispersion functions for the Maxwellian and Lorentzian distributions respectively as defined by *Fried and Conte* [1961] and *Summers and Thorne* [1992] with

$$\xi_j^{\pm} = \frac{\omega - k_\parallel v_{0j} \pm \Omega_j}{k_\parallel v_j}, \tag{4}$$

and κ_j and $v_{\kappa j}$ are the kappa index and thermal velocity of the jth components velocity distribution as defined by *Summers and Thorne* [1992].

Using this approach, the majority of events (12 of 18) for which LEPEDEA data is available can adequately be explained by linear Vlasov theory in terms of the observed frequency and polarization.

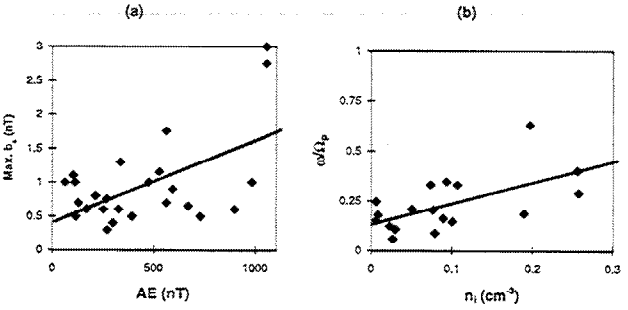

Figure 3. (a) The variation of maximum transverse wave amplitude with hourly average values of *AE* from the WDC-C2 for Geomagnetism at Kyoto University. (b) The variation of wave frequency, normalized by Ω_p, with total ion number density from LEPEDEA and FPE moment data.

It should be remembered however that these calculations are all based upon the assumption of local generation. That is, we are observing the wave in its source region. In this regard, there are some obvious exceptions. Those waves observed in the lobes prior to entry into the plasma sheet boundary layer invariably cannot be explained in terms of the Vlasov theory applied to the distribution function at the time of wave observation. This suggests that such waves have propagated some distance from their source [*Burinskaya et al.*, 1994], and hence the assumption of local generation breaks down. Further, the distribution data are averaged over a period of 8 min. Consequently, the parameters inserted into the dispersion relation are not always accurate representations of the plasma parameters at the commencement of a particular event.

4. Wave Burst Case Studies

The three case studies selected include observations made from the plasma sheet boundary layer through to the central plasma sheet and in addition to the case considered by *Chaston et al.* [1994] can be considered characteristic of polarized wave activity in the frequency range $\Omega_O^+ \leq \omega < \Omega_p$ through this region of near-Earth space. The location of each wave event with respect to its plasma environment (namely, plasma sheet, plasma sheet boundary layer, lobe, etc.) is identified by considering the proton distribution function observed by the spacecraft at the same time.

4.1. Ion Cyclotron Waves in the Plasma Sheet Boundary Layer

The streaming distributions of the plasma sheet boundary layer provide temperature anisotropies and relative drifts sufficient to excite several electromagnetic and electrostatic instabilities [*Angelopoulos et al.*, 1989; *Chaston et al.*, 1994; *Akimoto and Omidi*, 1986]. In this particular case the anisotropies of the beam components is sufficient to drive a Doppler-shifted cyclotron instability and provide wave growth for a right-hand polarized electromagnetic wave burst.

4.1.1. Wave observations: PSBL. Figure 4 is a montage illustrating the wave properties observed in the magnetic field data measured onboard ISEE 1 in field-aligned coordinates from 2000-2020 UT on April 27, 1978, when the spacecraft was located at (-15.46, 6.37, 12.32)R_E in the GSM coordinate system. The time series (Figure 4a) and dynamic power and polarization spectra (Figure 4b) indicate an enhancement of wave power coincident with a decrease in ambient magnetic field strength and entry into the plasma sheet boundary layer from the lobes at ~2003 UT. Maximum transverse wave power occurs at 65 mHz ($\omega/\Omega_p \approx 0.14$) and persists at this frequency until ~2009 UT. The band-pass (50-80 mHz) filtered results over this interval (Figure 4c) reveal wave amplitudes ~1 nT with $b_\parallel/b_\perp$ in the range 0.3-0.5 over the event duration. The hodograms (Figure 4d) reveal an average ellipticity of 0.23 in the components transverse (X-Y) to the field with suffi-

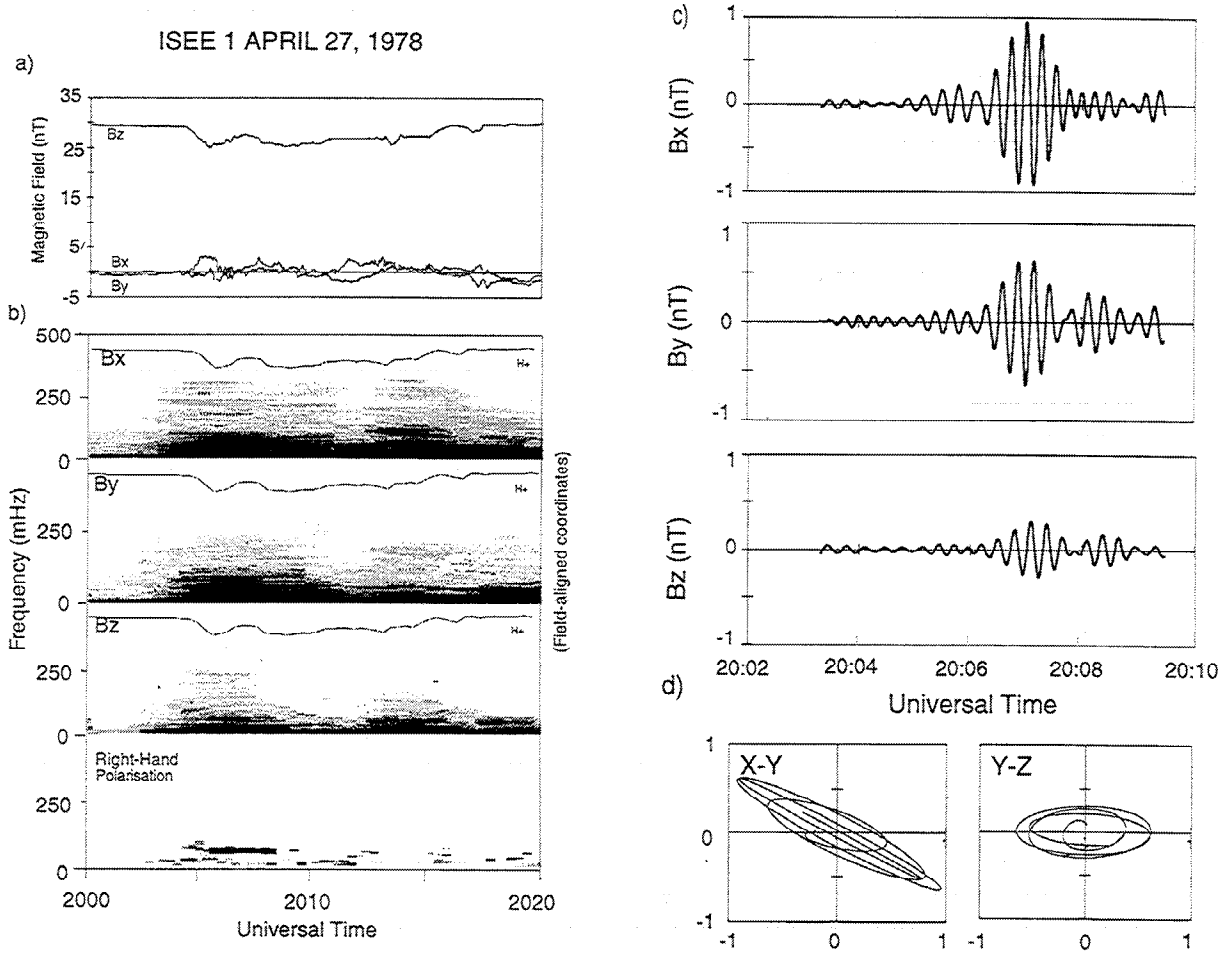

Figure 4. (a) ISEE 1 magnetic field time series and (b) spectra from 2000 to 2020 UT on April 27, 1978, in field-aligned coordinates with Z in the field-aligned direction. The darkest shading level corresponds to power spectral densities ≥ 1 nT^2/Hz. (c, d) Bandpass filtered (60-90 mHz) magnetic field time series and polarization hodograms from 2003 to 2010 UT.

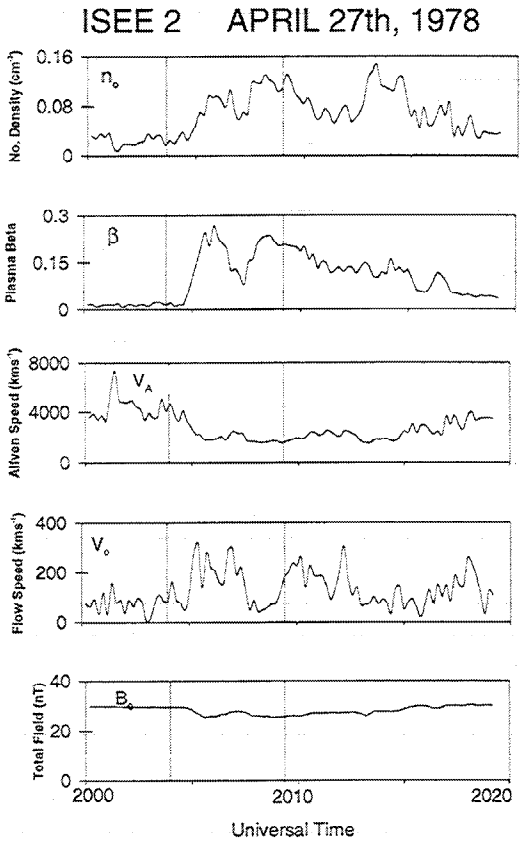

Figure 5. Plasma moment and magnetic field results from the FPE and fluxgate magnetometer experiments onboard ISEE 2 at 2010 UT on April 27, 1978. The resolution of the moment data is 12 s and for the field results 1 s.

cient regularity in the Y-Z hodogram to suggests that the longitudinal fluctuations are part of the same wave field or mode. Furthermore, by assuming a plane wave, minimum variance analysis yields θ_k=39° for this wave burst which is sufficient to explain the observed longitudinal component. The phasing between magnetic field observations on ISEE 1 and ISEE 2 implies a wavelength ~2400 km and indicates that the burst propagated earthward along the field.

4.1.2. Particle observations: PSBL. Figure 5 illustrates the bulk moment parameters as observed by the FPE and fluxgate magnetometer onboard ISEE 2, from 2000 UT until 2020 UT. Entry into the plasma sheet boundary layer from the northern tail lobes is indicated by increases in ion number density, plasma beta and flow speed at ~2005 UT. The observed sudden increase in these parameters, particularly plasma beta, was coincident with the commencement of a burst of enhanced polarized electromagnetic wave activity as discussed above and is indicated here by the vertical lines in Figure 5 extending from 2005 to 2009 UT. Over this interval there is a net increase in number density with no average change in β subsequent to the initial increase. The sunward proton flow speed is enhanced over the interval up to 300 kms^{-1} or 0.15 v_A but falls below 100 kms^{-1} over the event duration.

Figure 6 illustrates the proton and electron distribution functions as measured onboard ISEE 1 from 2003 to 2011 UT by the LEPEDEA experiment. Because of the length of observation and the proximity of the ISEE spacecraft at this time, these distributions represent the average distribution seen by both spacecraft over the duration of the wave burst event. The ion distribution is dominated by an incomplete shell arising from two opposed crescent shaped beam components. Inspection of the 8 s FPE ion distribution function microfiche plots at the commencement of the wave event (~2005 UT) confirm this. In addition a second antisunward traveling beam at -1415 km/s is evident as well as a cool core component which is obscured by the low-energy limit of the instrument in this case. The electron distribution is largely isotropic except for a wedge of acceleration at a pitch angle of 135°. Performing moment calculations over these distributions yields the parameters given in Table 2 where the assumption that all ion are protons is invoked. The values given for κ have been determined by applying a nonlinear fitting routine to the distribution function profile along $v_{\|}$.

4.1.3. Linear modeling: PSBL. Figure 7a illustrates the dispersion results obtained from the solution of (1) assuming a bi-Maxwellian functional form for each component in the distribution using the moment parameters given in Table 2. Three roots in ω/Ω_p occur with coupling between the positive helicity Alfven (ω_1,γ_1) and magnetosonic (ω_2,γ_2) branches for $kc/\omega_p \leq 1$ due to the earthward directed current associated with the electron drift. Consequently, the kink-like instability (also ω_1,γ_1) exhibits strong growth for both right- and left-hand polarized waves for $|\omega/\Omega_p| < 0.1$ with γ_{max}/Ω_p=0.49 at ω/Ω_p=-0.1 (left-hand polarized). The anisotropy of the earthward directed beam provides growth for the Doppler-shifted proton cyclotron wave (ω_1,γ_1) which exhibits left-hand polarization only, over $-0.27 \leq \omega/\Omega_p \leq -0.1$ with γ_{max}/Ω_p=0.08 at ω/Ω_p=-0.26. In the case of negative helicity the beam anisotropy provides the free energy for marginal growth above the background for left-hand polarized cyclotron waves (ω_1,γ_1), where γ_{max}/Ω_p=0.01 and $\omega/\Omega_p \approx 0.47$.

The equivalent dispersion results for a bi-Lorentzian distribution function are presented in figure 7b. Identical instabilities arise for both functional forms, however the dispersion characteristics of the growing wave modes for the bi-Lorentzian case are modified. The kink-like mode (ω_1,γ_1) shows almost no variation in growth rate, frequency or wavenumber from the bi-Maxwellian case and remains virtually unchanged by the choice of κ. This can be easily understood since this mode is not reliant upon wave-particle resonance and is largely unaffected by the thermal properties of the plasma. The proton anisotropy instability (also ω_1,γ_1) however, exhibits a lower maximum growth rate yet a larger range of unstable wavenumbers for the equivalent bi-Lorentzian form. Consequently, the wavenumbers unstable to the kink-like instability overlap with those where a significant portion of the beam ions are cyclotron resonant. As a result, the Alfven (ω_1,γ_1) and magnetosonic (ω_2,γ_2) branches decouple at smaller wavenumbers than in the bi-Maxwellian case and the positive helicity Alfven branch is continuously unstable from kc/ω_p=0 to 2.5. This extended range of unstable wavenumbers provides growth for predominately

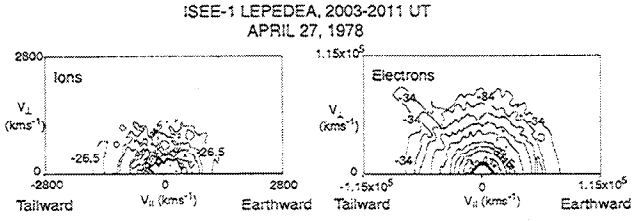

Figure 6. ISEE 1 LEPEDEA proton and electron velocity distribution function for April 27, 1978, averaged over 2003-2011 UT. Here $v_{\|}$ and $v_{\perp}$ indicate velocities parallel and perpendicular to the background magnetic field respectively ($f(v_{\|},v_{\perp})$ in $cm^{-6}s^3$). The minimum contour for protons and electron corresponds to $\log_{10}(f)$=-26.5 and - 34.0 respectively and the contour interval in both cases is 0.5.

Table 2. Normalized Moment Parameters for the Ion and Electron Distributions From 2003 to 2011 UT of Figure 6.

Parameter	Cold Protons (core) $\kappa\approx3$	Parallel (Earthward) Beam Protons $\kappa\approx2$	Antiparallel (Tailward) Beam Protons $\kappa\approx2$	Second Antiparallel Beam Protons $\kappa\approx3$	Electrons $\kappa\approx3$
n_j/n_t	0.012	0.57	0.37	0.048	1
$T_{\perp j}/T_{\parallel j}$	5.81	7.71	12.1	24.0	1.7
$T_{\perp j}/T_{\perp c}$	1	8.1	16.2	12.2	3.4
v_{0j}/v_A	-0.073	0.33	-0.35	-0.79	-1.0

Here n_t=0.0013 cm^{-3}, $T_{\perp c}$=248.7 eV and B_0=27 nT.

left-hand polarized waves except at the point where the two branches decouple where right-handed wave growth occurs for frequencies $\omega/\Omega_p<0.1$.

Comparing the observed wave data with the modeling results indicates reasonable agreement over the frequency range where growth is predicted. From Figure 4, the wave data indicated a band of enhanced polarized wave activity from 50 to 80 mHz or ω/Ω_p=0.1-0.17 with wavelength ~2400 km or $kc/\omega_p\approx1.8$. This range falls within the frequencies and wavenumbers of significant positive growth for the positive helicity branch of the proton cyclotron anisotropy instability (ω_1,γ_1) for both bi-Maxwellian and bi-Lorentzian distribution functions as modeled. However, the predicted and observed wave polarizations disagree except over a very narrow wavenumber range $0.85\le kc/\omega_p\le1.05$ where right-hand polarization is predicted. Significantly, this narrow range represents the only portion of wave growth for waves which propagate in the earthward direction as observed.

4.2. Ion Cyclotron Waves in the inner Plasma Sheet Boundary Layer

With penetration towards the plasma sheet, proton distributions become increasingly shell-like [*Elphic and Gary*, 1990]. Here the

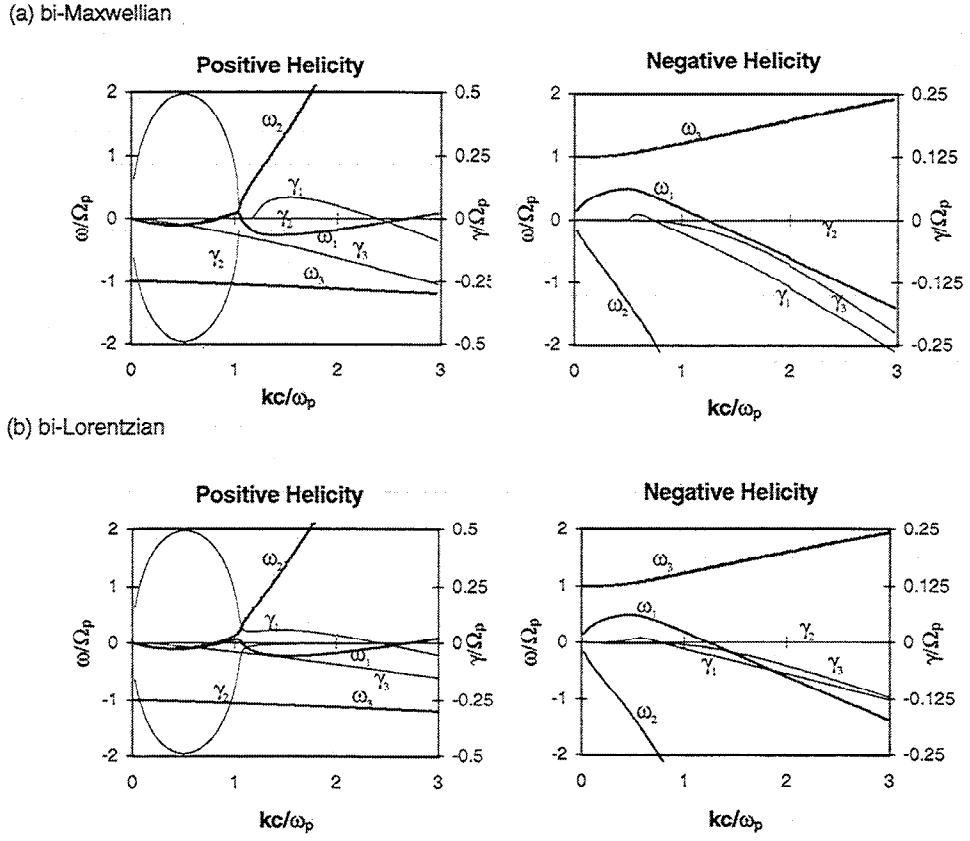

Figure 7. Solutions to the linear dispersion relation (1) for (a) bi-Maxwellian and (b) bi-Lorentzian distributions using the parameters of Table 2. The darker curves correspond to real frequencies (ω) and the lighter curves to growth rates (γ). The curves labeled ω_1 and γ_1 represent the Alfven branch below Ω_p, ω_2 and γ_2 represent the magnetosonic branch and ω_3 and γ_3 represent the Alfven branch above Ω_p.

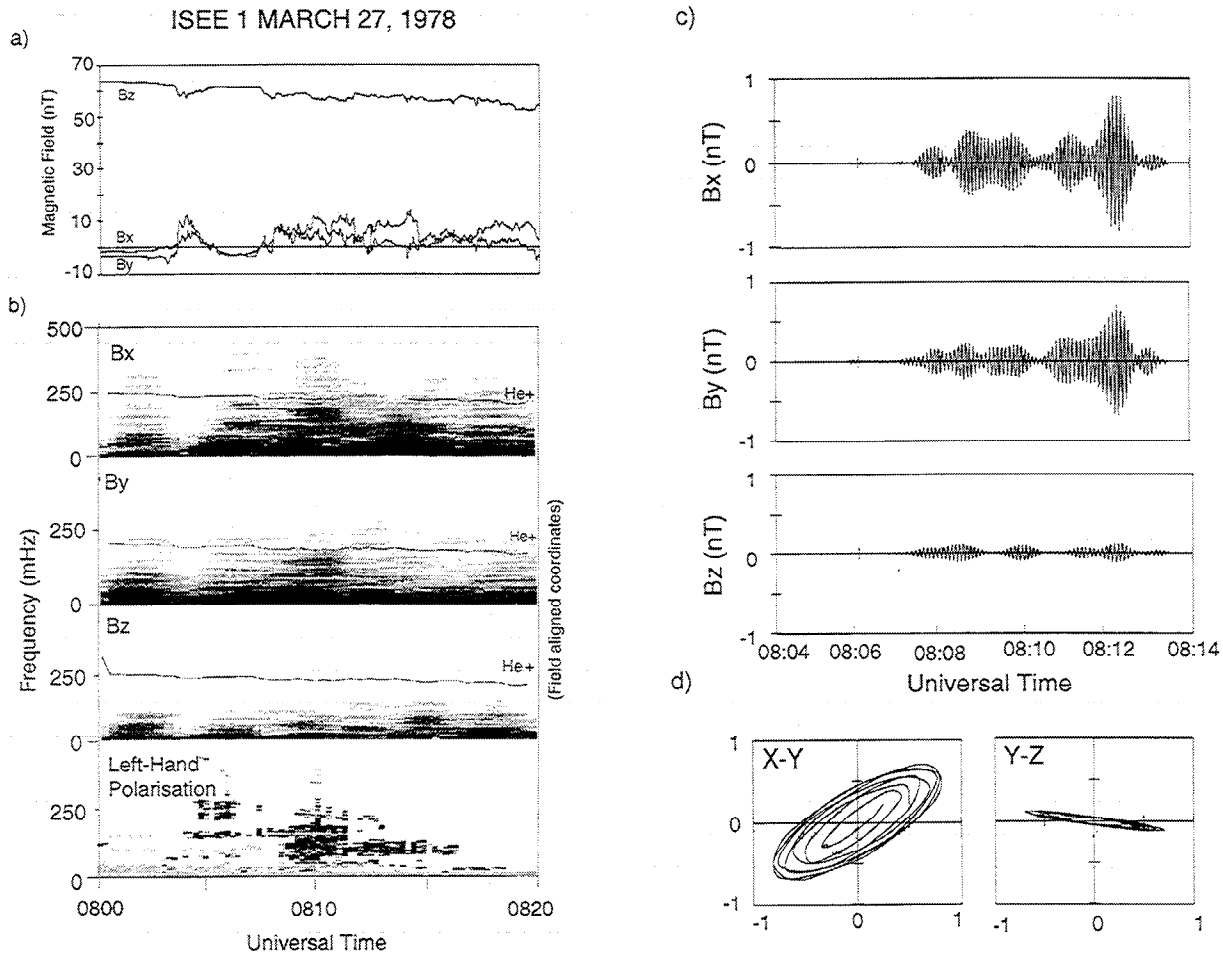

Figure 8. (a) ISEE 1 magnetic field time series and (b) spectra from 0800 to 8020 UT on March 27, 1978, in field-aligned coordinates with Z in the field-aligned direction. The darkest shading level corresponds to power spectral densities ≥ 1 nT^2/Hz. (c, d) Bandpass filtered (160-190 mHz) magnetic field time series and polarization hodograms from 0805 to 0814 UT.

approach of *Gary and Sinha* [1989] for full shell distributions is adopted to explain the occurrence of a wave burst on the very boundary between the plasma sheet boundary layer and plasma sheet.

4.2.1. Wave observations: Inner PSBL. Figure 8 is a montage illustrating the wave properties observed in the magnetic field data measured onboard ISEE 1 in field-aligned coordinates from 0800 to 0820 UT on March 27, 1978, when the spacecraft was located at (-12.54, 2.93, 6.51)R_E in the GSM coordinate system. The time series (Figure 8a) and dynamic power and polarization spectra (Figure 8b) indicate a band of polarized transverse wave activity at ~1805 UT extending from 50-250 mHz and continuing until 0817 UT with decreasing frequency over this interval. The filtered magnetic field time series (Figure 8c) (160-190 mHz) show a maximum transverse amplitude of ~0.7 nT with $b_\perp$ typically ~0.5 nT. The compressional component has a maximum amplitude of 0.15 nT. The X-Y (Figure 8d) hodogram indicates an ellipticity of -0.5. The Y-Z hodogram demonstrates the largely transverse nature of the wave activity but still indicates coherency between the compressional and transverse components. Application of principal axis analysis to these data yields a wavenormal angle θ_k= 13.5° and again the small compressional component can be explained from the slight off-parallel propagation of the plane wave. Phase analysis from observations made onboard ISEE 1 and ISEE 2 indicate that the wave propagated earthward parallel to the field with a wavelength of ~6000 km.

4.2.2. Particle observations: Inner PSBL. Unfortunately, the FPE was not operational over the interval to be considered here so we shall rely exclusively upon the distribution function data from the LEPEDEA experiment onboard ISEE 1. Figure 9 illustrates the ion and electron distribution functions as phase space density contour plots from 0758 until 0814 UT when the spacecraft was located at ~(-12.38, 2.93, 6.48)R_E in the GSM system. First, consider the ion distributions. Over the interval from 0758 to 0806 UT the majority of the ions are contained in a single complete shell with radius 1141 km/s and average temperature 233.1 eV with a slight tailward drift of 100.5 km/s antiparallel to the background field. A suprathermal proton core component is also apparent with temperature $T_\perp$=562.4 eV and $T_\parallel$=136.7 eV and is virtually stationary in the spacecraft frame. From 0806 to 0814 UT the spacecraft traveled towards the plasma sheet and the total ion number density increased from 0.027 to 0.077 cm^{-3}. The empty portion of phase space between the outer shell and the core filled in during this transition and the total distribution tended towards the hot isotropic single component characteristic of the central plasma sheet.

The electron distributions over the same interval are in this case the most important species in controlling the stability of the plasma. Since the shell distributions considered have only small

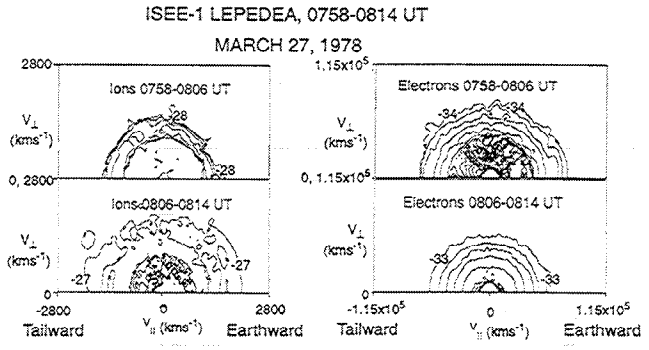

Figure 9. ISEE 1 LEPEDEA proton and electron velocity distribution function for March 27, 1978, averaged over 0758-0806 and 0806-0814 UT. Here $v_{\parallel}$ and $v_{\perp}$ indicate velocities parallel and perpendicular to the background magnetic field respectively ($f(v_{\parallel},v_{\perp})$ in $cm^{-6}s^3$). The minimum contour for protons and electron corresponds to $\log_{10}(f)$=-28 and -34, respectively and the contour interval in both cases is 0.5.

drift speeds they are stable to electromagnetic field fluctuations [*Gary and Sinha*,1989; *Freund and Wu*, 1988]. Furthermore, the temperature of the core distribution is not sufficient to excite the anisotropy instability. Consequently, the only instability viable under these circumstances is the kink-like mode driven by relative electron/ion drift. In this regard, the irregular electron distribution over the interval 0758-0806 UT has a drift speed in the spacecraft frame of -5742.1 km/s providing an ion/electron relative drift speed of -1.2 V_A. From 0806 to 0814 UT the irregularity of the electron distribution is removed perhaps through the emission of whistler or electrostatic waves [*Zhang et al.*, 1993] such that the electron drift falls to -675 km/s or a relative ion/electron drift speed of 0.14 V_A.

The moment parameters for both these distributions are presented in Table 3 and 4 together with the shell indices as defined by *Gary and Sinha* [1989]. Since the wave event commenced at ~0805 UT, we adopt the parameters from 0806 to 0814 UT for modeling. However, since the electron drift changes rapidly under the influence of the kink-like mode [*Gary and Winske*, 1990], the electron drift from 0758-0806 UT is employed.

4.2.3. Linear modeling: Inner PSBL. For simplicity, in this case we consider only the dispersion results for distributions modeled as bi-Maxwellians with the modifications given by *Gary and Sinha* [1989] to provide the observed shell configuration. These results are presented in Figure 10.

The positive helicity dispersion curves are dominated by the effects of the field-aligned current. Over the range of wavenumbers $0<kc/\omega_p<1.2$ the kink-like mode (ω_1,γ_1) provides strong growth for left-handed tailward (antiparallel) propagating waves over the frequency range $0>\omega/\Omega_p>-0.184$ with maximum growth rate $\gamma_{max}/\Omega_p=0.56$ at frequency $\omega/\Omega_p=-0.18$ and wavenumber $kc/\omega_p=0.6$. This is the only growing electromagnetic mode present in the plasma at this time, including those wave modes arising from the negative helicity solutions to the dispersion relation.

Comparison of these results with the observed event wave data indicates agreement in both wave frequency and polarization. The observed band of polarized fluctuations at 0805 UT extends from 50-250 mHz or $0.05<\omega/\Omega_p<0.27$, the majority of which falls within the range of large positive growth for the kink-like instability. The observations indicate left-hand polarization (ellipticity=-0.5) in agreement with the polarization state of the modeled kink-like mode (ω_1,γ_1 in the positive helicity case). Furthermore, the relative observations made from ISEE-1 and ISEE-2 indicate that the waves propagate tailward with $kc/\omega_p=0.86$ for fluctuations in the range 160-190 mHz. From the dispersion curves at wavenumber $kc/\omega_p=0.86$ the kink-like mode has wave frequency 140 mHz with $\gamma/\gamma_{max}=0.9$, and also propagates tailward. Although this agreement is not exact it certainly falls within the error margin provided by the uncertainty in the moment parameters. For example, if the relative ion/electron drift was -1.3 v_A instead of -1.2 v_A, then the frequency at wavenumber $kc/\omega_p=0.86$ would fall within the range 160-190 mHz as observed. Alternatively, if we adopt the electron drift from the interval 0806-0814 UT given in Table 4 (i.e., -0.7 v_A) the instability contracts to frequencies $\omega/\Omega_p<0.1$ and wavenumbers $kc/\omega_p<0.2$ consistent with the observed decreasing frequency of the emission from 0805 UT to 0815 UT.

4.3. Ion Cyclotron Waves in the Central Plasma Sheet

Particle distributions in the central plasma sheet are considerably simpler than the streaming distributions characteristic of the plasma populating the plasma sheet boundary layer. Nonetheless, for brief periods of time, perhaps under the influence of low-frequency (Pc5) field perturbations, ion distributions in this region of space may be perturbed sufficiently from electromagnetic stability to provide growth for ion cyclotron waves. Since ion distributions here have temperatures of the order of 5 keV and densities up to 1 cm^{-3}, the anisotropy required to drive the plasma unstable is significantly less than that required in the boundary layer. Here we consider such an occurrence where the temperature anisotropy of the plasma in the central plasma sheet leads to an ion cyclotron wave burst.

4.3.1. Wave Observations: PS. On April 2, 1978, at 1848 UT ISEE 1/2 were located at (-13.72, -5.19, 2.10)R_E in the GSM coordinate system and in the central plasma sheet. Figure 11a illustrates the magnetic field observed onboard ISEE 1 from 1840 to 1900 UT. In this case there is an enhancement of activity in the transverse field components coincident with the decrease of the total field commencing at ~1845 UT. Before considering the spectral results associated with these observations it should be emphasized that the sudden decrease in field strength in the Z component at ~1850 is independent of the appearance of transverse wave activity over this interval. That is, the transverse wave activity we consider is not a spectral component of the spiky background field at this time.

Figure 11b shows the dynamic power and polarization spectra in field-aligned coordinates calculated over the same 20-min inter-

Table 3. Normalized Moment Parameters for Each Component Present in the Ion and Electron Distribution from 0758 to 0806 UT of Figure 9.

Parameter	Core Protons	Inner Shell Protons	Outer Shell Protons	Electrons
n_j/n_t	0.08	0.39	0.53	1
$T_{\perp j}/T_{\parallel j}$	9.6	1	1	1.75
$T_{\perp j}/T_{\perp c}$	1	0.6	4.3	3.9
v_{0j}/v_A	-0.035	-0.031	-0.021	-1.2

Here n_t=0.027 cm^{-3}, $T_{\perp c}$=562.4 eV, B_0=62 nT, and n_{shell}=13.

Table 4. Normalized Moment Parameters for each Component Present in the Ion and Electron Distribution From 0806 to 0814 UT of Figure 9.

Parameter	Core Protons	Shell Protons	Electrons
n_j/n_t	0.07	0.93	1
$T_{\perp j}/T_{\parallel j}$	4.1	1	1.76
$T_{\perp j}/T_{\perp c}$	1	0.83	3.03
v_{0j}/v_A	0	0.012	-0.7

Here n_t=0.077 cm^{-3}, $T_{\perp c}$=369.4 eV, B_0=60 nT and $n_{inner\ shell}$=9; $n_{outer\ shell}$=8.

val. The enhanced transverse wave activity identified above can be seen here to extend initially over a bandwidth from 200 to 250 mHz with decreasing frequency synchronous with the decrease in the ambient field strength and Ω_p. By 1855 UT the frequency of the wave activity had fallen to below 125 mHz and remains below Ω_p. Peak power for these transverse waves occurs at ~240 mHz ($\omega/\Omega_p \approx 0.6$). Comparison of the wave power and polarization spectra indicate a correlation between the observed bandwidth of transverse wave activity and the band of left-hand polarized wave power extending over the same interval. Further the decreasing frequency of the wave activity is reflected in the decreasing frequency of the left-hand polarized wave band.

Figure 11c illustrates the magnetic field components filtered over the range from 200 to 250 mHz over the interval from 1848 to 1852 UT. The bursty nature of the activity is again evident in this event with a wave envelope spanning approximately ~2 min in this frequency range. Also, the transverse components exhibit the largest amplitudes with maximum and averaged wave amplitudes of 1.5 and 0.7 nT, respectively. The compressional component is significantly smaller with a maximum amplitude of 0.5 nT and averaged amplitude of 0.3 nT. The polarization hodograms presented in Figure 11d indicate almost circular polarization with an ellipticity of -0.8 in the X-Y plane. The Y-Z hodogram in this case is irregular in form suggesting the presence of an additional compressional mode. Application of principal axis analysis to the filtered field fluctuations over 200-250 mHz from 1849 to 1851 UT indicates a wavenormal angle for these perturbations of θ_k=18.7°. The same analysis performed over the band 40-70 mHz from 1853 to 1855 UT yields a wavenormal angle of θ_k=38.3°. This indicates increasing wave growth at oblique angles with decreasing frequency over the duration of the wave event. Including the observations made from ISEE 2 suggests that the observed wave is traveling earthward or parallel to $\mathbf{B_o}$ with an approximate wavelength of 4000 km.

4.3.2. Particle observations: PS. Since the plasma data from the ISEE 2 FPE experiment is not available over this interval we again rely upon the LEPEDEA distribution function measurements. In this regard Figure 12 illustrates the average ion and elec-

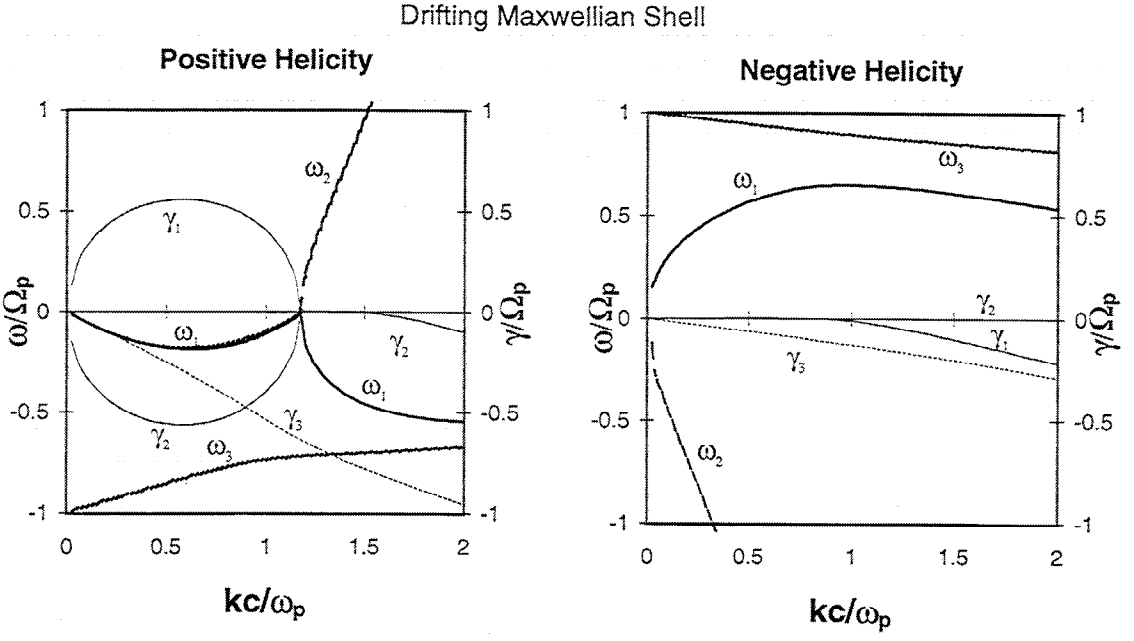

Figure 10. Solutions to the linear dispersion relation (1) for bi-Maxwellian and proton shell distributions using the parameters of Table 3. The darker curves correspond to real frequencies and the lighter curves to growth rates. The curves labeled ω_1 and γ_1 represent the Alfven branch below Ω_p, ω_2, and γ_2 represent the magnetosonic branch and ω_3 and γ_3 represent the Alfven branch above the Doppler shifted proton resonance.

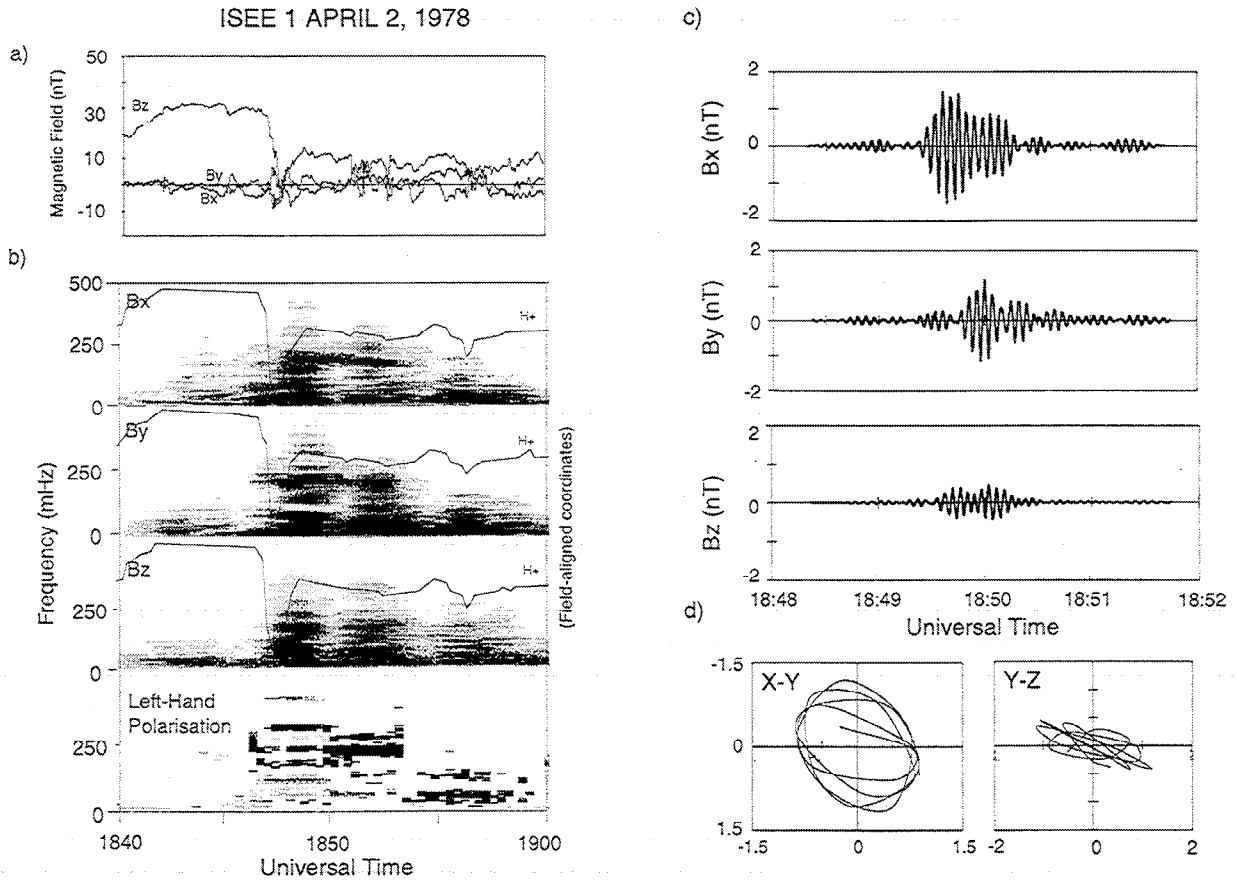

Figure 11. (a) ISEE 1 magnetic field time series and (b) spectra from 1840 to 1900 UT on April 2, 1978, in field-aligned coordinates with Z in the field-aligned direction. The darkest shading level corresponds to power spectral densities ≥ 1 nT^2/Hz. (c, d) Bandpass filtered (200-250 mHz) magnetic field time series and polarization hodograms from 1848 to 1852 UT.

tron distribution functions as measured by this experiment over the period 1848-1856 UT. The ion distribution contains a single almost isotropic component with virtually no drift in the spacecraft frame as expected of plasma sheet distributions [*Eastman et al.*, 1984]. Similarly, the electron distribution is relatively hot and isotropic. Table 5 represents the results of moment calculations performed over these distributions where a simple two component plasma is assumed. In this case the thermal energy of the ion distribution is made available for wave growth through the anisotropy, albeit small, of the single hot ion component.

4.3.3. Linear modeling: PS. Invoking the assumption that all ions are protons, the dispersion curves in this case have the rather simple form illustrated in Figure 13. Since the component drifts are small the positive and negative helicity curves are close to symmetric. Both provide moderate growth for left-hand polarized oscillations on the Alfven branch (ω_1,γ_1). Due to the slight tailward current arising from the proton drift the kink-like mode appears for wavenumbers $kc/\omega_p<0.5$ providing weak growth for an essentially nonoscillatory mode.

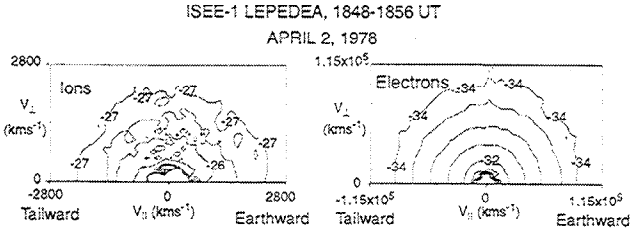

Figure 12. ISEE 1 LEPEDEA proton and electron velocity distribution function for April 2, 1978, averaged over 1848-1856 UT. Here $v_{||}$ and $v_\perp$ indicate velocities parallel and perpendicular to the background magnetic field respectively ($f(v_{||},v_\perp)$ in $cm^{-6}s^3$). The minimum contour for protons and electron corresponds to $\log_{10}(f)$=-27 and -34, respectively, and the contour interval in both cases is 0.5.

Table 5. Normalized Moment Parameters for the Ion and Electron Distributions From 1848-1856 UT of Figure 12.

Parameter	Protons, κ≈2	Electrons,κ≈2
n_j/n_t	1	1
$T_{\perp j}/T_{\|j}$	2.12	1.32
$T_{\perp j}/T_{\perp c}$	1	0.272
v_{0j}/v_A	-0.095	0.013

Here n_t=0.197 cm^{-3}, $T_{\perp c}$=2749.1 eV, and B_0=10 nT.

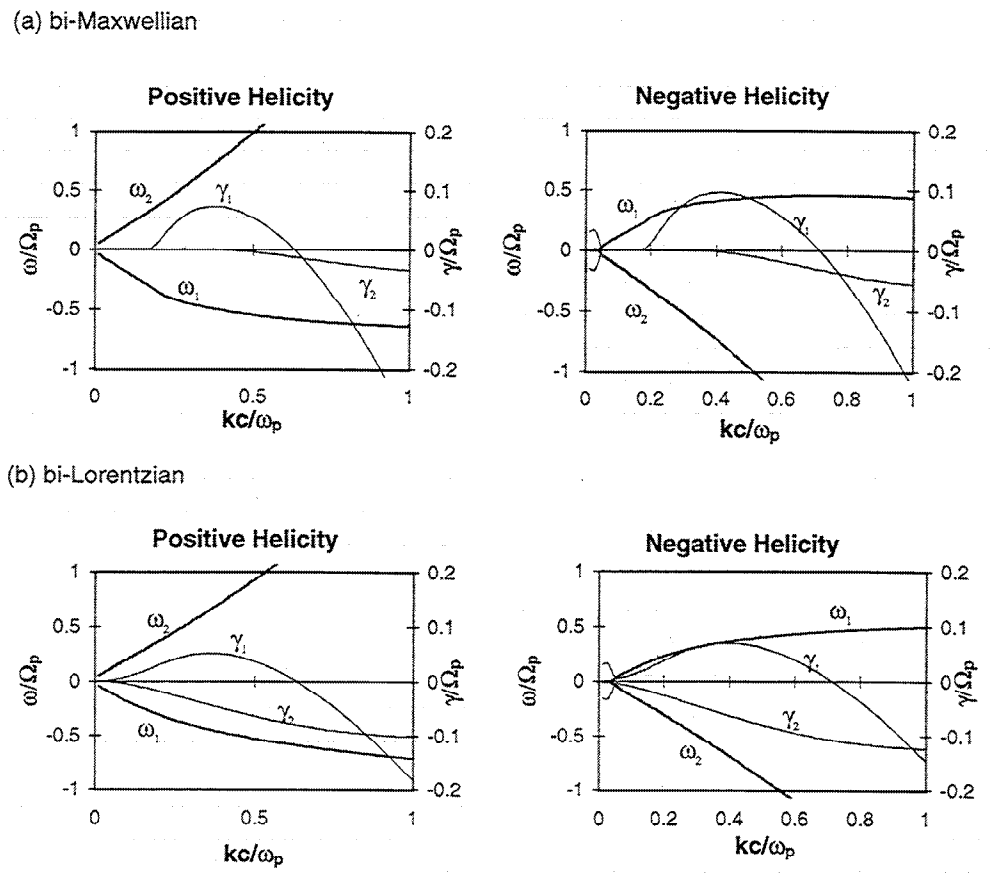

Figure 13. Solutions to the linear dispersion relation (1) for (a) bi-Maxwellian and (b) bi-Lorentzian distributions using the parameters of Table 4. The darker curves correspond to real frequencies and the lighter curves to growth rates. The curves labeled ω_1 and γ_1 represent the Alfven branch and ω_2 and γ_2 represent the magnetosonic branch.

If we, first, consider the results obtained by modeling each component as bi-Maxwellian (Figure 13a) for the negative helicity branch (ω_1,γ_1), a region of significant growth extends over wavenumbers $0.2<kc/\omega_p<0.7$ for frequencies $0.27<\omega/\Omega_p<0.6$ with $\gamma_{max}/\Omega_p=0.096$ at $kc/\omega_p=0.42$ and $\omega/\Omega_p=0.42$. In the bi-Lorentzian case (Figure 13b), because of the extended width of the resonance for the anisotropy instability (ω_1,γ_1), significant growth extends over a slightly larger wavenumber range with $0.1<kc/\omega_p<0.7$ and lower frequency range with $0.1<\omega/\Omega_p<0.45$. The large value of plasma beta for the unstable proton component however yields generally lower growth rates over this range than indicated for the bi-Maxwellian case with $\gamma_{max}/\Omega_p= 0.07$ at $kc/\omega_p=0.4$ and $\omega/\Omega_p=0.36$. Because of the extremely low frequency of the kink-like mode in this case it is unlikely to provide any observable field fluctuations within the time scale for instability saturation.

There is general agreement between the magnetic field fluctuations observed over the same interval spanned by the distribution function data above with the predictions of the linear Vlasov theory applied to these data. The wave observations indicate left-hand polarized field fluctuations which vary in frequency from 250 mHz to below 125 mHz over the period from 1848 to 1856 UT. These frequencies approximately satisfy $\omega/\Omega_p\leq 0.5$ throughout and consequently fall within the region of significant positive growth for the anisotropy instability (ω_1,γ_1). This is particularly so for the negative helicity mode which provides larger growth than its positive helicity counterpart and propagates earthward parallel to $\mathbf{B_o}$ consistent with the observed direction of propagation. The approximate wavelength of >4000 km yields wavenumbers of $kc/\omega_p<0.8$ in agreement with the wavenumber range covered by the anisotropy instability in this case.

5. Discussion

5.1. Unpolarized Wave Activity: Broadband Magnetic Noise?

The character of the polarized events we have identified here is significantly different to that of the largely unpolarized/incoherent (according to the "degree of polarization" criteria mentioned in section 2) activity which seems to dominate most of the field fluctuations observed through these regions of space. One aspect in particular that distinguishes the nature of the polarized activity from the background noise is the form of the static power spectra. As reported by *Russell and McPerron* [1972] and later by *Bauer et al.* [1995], the low-frequency magnetic noise follows a power law ($P\sim\omega^{-\alpha}$; $2<\alpha<2.5$) which does not exhibit any structure near Ω_j. However, as indicated in spectral results presented above, the polarized events considered exhibit spectral peaks over the band where coherent transverse wave activity occurs. Consequently, the wave amplitude of this bursty polarized activity is significantly larger than that of the unpolarized activity over the same frequency band. This suggests a local source for the wave generation where the assumption of spatial homogeneity within one wavelength of the spacecraft at the time of observation may be valid.

Since the linear Vlasov theory considered predicts only left- or right-handed polarization, what then is the source of the largely unpolarized transverse wave activity? The source or more probably the sources of this pervasive low frequency magnetic noise are

difficult to discern. However, such activity is certainly not unexpected for the turbulent plasmas populating these regions. The statistical study performed by *Bauer et al.* [1995] suggests several possible source mechanisms for this noise based on correlation between enhanced wave activity and the temporal variation in plasma moment parameters. For unpolarized activity, perhaps the identification of a specific source mechanism is somewhat naive because it requires the assumption that the wave is observed in the source region. Ray tracing studies indicate that the polarized characteristics of a propagating wave may be altered significantly away from the source region [*Rauch and Roux*, 1982; *Dowdell et al.*, 1995]. Furthermore, the superposition of multiple modes over a band of frequencies which may have propagated over varying distances before observation may provide the observed broadband spectra. Indeed, judging from the turbulent nature of these regions, it is more likely that such activity results from a combination of velocity space and spatial gradient instabilities rather than one mechanism alone. Perhaps the theoretical approach where circular polarization and spatially uniform distributions maintaining a regular bi-Maxwellian, bi-Lorentzian, or other form are part of the initial assumptions, can really only give a rough indication of the rather complicated wave-particle interactions occurring in these regions, especially where the wave activity is noise-like.

5.2. Bi-Maxwellian/bi-Lorentzian

Fitting a drifting bi-Lorentzian distribution of the form given by *Chaston et al.* [1997] to the unstable components in the plasma for each of the events listed in Table 1 yields κ values in the range from 2 to 10. Noticeable changes in wave dispersion and temporal growth occur for $\kappa \leq 4$. However, for the wave events modeled these changes are found to be insufficient to alter the linear stability of the plasma to the observed wave modes since in most cases the plasma is well above the threshold for the anisotropy instability. Furthermore, the unstable frequency range is sufficiently broad to include the observed frequency range despite some shifting with changes in κ. However, as demonstrated by *Chaston et al.* [1997] there may be important changes in convective growth rates as κ is decreased to less than 4. This occurs because the bi-Lorentzian instability extends over a broader range in kc/ω_p (as can be seen in Figures 7 and 13) that may include additional wavenumbers where the group velocity, $\partial\omega/\partial k$, approaches zero. From Figure 7 it can be seen that group velocity of the growing positive helicity mode passes through zero at $kc/\omega_p \approx 0.5$, 1.0 and 1.4. For the bi-Maxwellian case the temporal growth at $kc/\omega_p \approx 1.0$ is much less than for the bi-Lorentzian and in fact approaches zero where $\partial\omega/\partial k \rightarrow 0$. A simple calculation at this wavenumber ($\gamma/(\partial\omega/\partial k)$) shows that the bi-Lorentzian distribution provides a convective growth rate an order of magnitude larger than the bi-Maxwellian distribution. Significantly, the observations discussed previously for this event indicate that based on the wave polarization and direction of propagation it is at this wavenumber that the wave is observed.

The extension of the width of the instability in wavenumber associated with applying the bi-Lorentzian distribution also provides a broader range in frequency over which the instability operates. Both Figures 7 and 13 demonstrate that invoking the bi-Lorentzian distribution provides wave growth continuously over the range $0 < |\omega/\Omega_p| < 0.4$. This may to some degree explain the more commonly occurring broadbanded nature of most of the wave activity seen in these regions with $\omega < \Omega_p$ as was discussed in the previous section.

5.3. Alternative Instabilities

At no stage in the spacecraft frame did the beam velocities observed exceed v_A. As a consequence neither the resonant or nonresonant beam instabilities are possible candidates exciting field perturbations in this region of space [*Gary and Shriver*, 1987]. Furthermore, this study did not extend to include the possibility of drift modes in the plasma associated with density or temperature gradients which may provide growth over the same frequency range. Essentially, drift waves are electrostatic, and the lower hybrid drift instability has been identified as one of the sources of broad band electrostatic noise in the plasma sheet boundary layer [*Schriver and Ashour Abdalla*, 1987]. However, for the values of plasma beta occurring in the plasma sheet and plasma sheet boundary layers the electrostatic drift mode may couple to the shear or compressional Alfven wave and hence provide an alternative mechanism to explain the observed electromagnetic waves. *Kuznetsova and Nikutowski* [1994] investigated this possibility in the near-Earth neutral sheet. Despite these results the application of the drift wave instability to explain magnetic field fluctuation should be treated with caution. *Hasegawa* [1975] points out the sensitivity of the drift wave to plasma parameters. In the inner magnetotail where $\beta \approx 0.1$ significant ion Landau damping limits the drift wave excitation of an Alfven wave to $k_\perp >> k_\parallel$ (compressional). In addition the electrostatic drift mode is stabilized by even a small fraction of cold electrons for Alfven waves where $k_\parallel > k_\perp$ (shear). So, while the plasma populating the plasma sheet and plasma sheet boundary layer may not be completely homogeneous, velocity space instabilities are the more likely candidate to explain polarized magnetic field fluctuations observed here particularly when their occurrence is so localized.

5.4. Pc3-Pc5 Interaction

An interesting feature of the majority of wave events identified is the decrease in background field strength that precedes the onset of transverse wave activity. This feature has been previously commented upon in a more general sense by *Russell and McPherron* [1972] and *Bauer et al.* [1995] and for specific case studies by *Angelopoulos et al.* [1989] and *Chaston et al.* [1994]. This is similar to observations on the dayside where enhanced ion cyclotron wave activity occurs during the decreasing phase of magnetic field changes [*Barfield and Coleman*, 1970; *Fraser et al.*, 1992]. From the FPE data available it appears that these decreases are synchronous with the enhancement of energetic proton flux. Furthermore, where continuous low-frequency (~Pc5) magnetic field fluctuations are present the bursts of Pc3 activity occur coincident with the decreasing phase of the Pc5 wave. If the Pc3 activity can be attributed to the kink-like and proton cyclotron anisotropy instabilities then it appears that the very low frequency field variations modulate the growth rate of the anisotropy and kink-like instabilities such that the wave bursts occur during that phase where the field strength is decreasing.

Theories to explain the similar modulation of ion cyclotron waves arising from hot ring current ions have been developed. *Coroniti and Kennel* [1970] provided a theory in which proton anisotropy variations occurred through an adiabatic process whereby the anisotropy of the energetic ions increases during the increasing field strength or the increasing phase of the low-frequency Pc5 wave. According to this theory, enhanced ion cyclotron wave activity may be expected during field increases. This is, however, in contradiction to what is observed here. Y. D. Hu and

B. J. Fraser (Compressional Pc5 wave, ring current ion, and electromagnetic ion cyclotron wave interactions, submitted to *Journal of Geomagnetics and Geoelectricity*, 1997) present a general theory which more closely explains observations. They suggest that the dominant contribution to the observed modulation in dayside magnetosphere observations is not anisotropy changes but rather the variation in the energetic ion flux and the associated decrease in magnetic field strength which enhances instability of the plasma to electromagnetic waves in general. This appears to be consistent with our observations. Essentially, since the rate of change in B_o and the frequency of the excited transverse waves are well separated, the interaction between the two can, at least to a first approximation, be considered independently. Application of the linear theory in this case with parameters increasing in energetic ion number density and falling in field strength yield enhanced growth rates for the anisotropy instability. Conversely, decreasing energetic ion number density and rising field strength yield progressively smaller growth rates. In this way those electromagnetic instabilities providing growth in the Pc3 range are modulated in antiphase with lower- frequency field changes, including Pc5 waves, in agreement with observations.

The enhancement of wave activity in the Pc3 range due to slow field changes has fundamental importance for magnetotail dynamics since it provides a means for the transfer of energy associated with large scale or global turbulence to smaller scales sizes. Since the wavelengths of the Pc5 activity (several R_E) are comparable to the scale size of the near-Earth magnetotail they relate directly to the energy input supplied to cause turbulence in the magnetotail. The wavelengths of the electromagnetic wave activity in the vicinity of Ω_p as presented in Table 1 are typically less than 1 R_E and, as *Bauer et al.*, [1995] indicates, such scale sizes correspond to the inertial range in the near-Earth magnetotail environment. Perhaps then, we are observing the cascade of energy to shorter scale lengths from the large-scale fluctuations as the tail is perturbed by the solar wind. In a general sense then, by studying the wave-particle-wave interactions of turbulence associated with very large scale phenomena down to the small scale sizes associated with particle heating we can better understand how solar wind energy in the magnetotail is dissipated.

In a more immediate sense the Pc3/Pc5 interaction provides one explanation for the bursty nature of the wave activity. However, in those cases where decreases in field strength are not accompanied by field increases bracketing the beginning and the end of the burst or wavepacket, what is mechanism which limits the wave activity to bursts? (This problem will be addressed using the quasi-linear theory of electromagnetic instability in a future paper.)

6. Conclusion

In this study the characteristics of polarized transverse electromagnetic wave bursts observed from ISEE 1/2 in the near-Earth magnetotail have been investigated. It has been found that these waves have properties characteristic of ion cyclotron waves suggesting the operation of field-aligned electromagnetic instabilities because of the following:

The duration of these bursts ranges from 3 to 10 min with this time independent of wave frequency. These times normalized in terms of Ω_p are consistent with saturation times expected for the proton anisotropy instability under the conditions prevalent in the plasma sheet boundary layer [*Gary and Winske*, 1990].

The wave frequency for nearly all events falls within the range 50-150 mHz. Invariably, these frequencies are below Ω_p and typically in the range ω/Ω_p=0.1-0.5. This suggests the strong possibility of resonant wave-particle interaction particularly under the influence of the Doppler shift provided by the beam components pervading this region of space.

Nearly all wave events obey $\theta_k<45°$ with most satisfying $\theta_k<25°$, in the spacecraft frame. If the wave is observed in the vicinity of the source, this implies that wave growth occurs preferentially for field fluctuations roughly in the direction parallel/antiparallel to the magnetic field, $\mathbf{B_o}$. In the cyclotron resonant case, this is consistent with the operation of the proton anisotropy instability. Also, in the non-resonant case electromagnetic instabilities such as the kink-like instability [*Gary et al.*, 1976] preferentially excite waves along the field.

The ratio of compressional to transverse wave amplitude is typically < 0.5 and varies linearly with θ_k indicating the plane nature of the wave bursts. This is as expected for waves generated by electromagnetic instabilities.

The majority of events are left-hand polarized in the spacecraft frame with the modulus of the ellipticity < 0.6. From theory we know that because of the Doppler shift provided by the beam components dominating this region of space, an individual field-aligned instability may provide both right- or left-hand polarization in the spacecraft frame. For the proton anisotropy instability, however, left-hand polarization is the dominant state for beam velocities less than v_A. In the case of the kink-like instability the polarization state is dependent upon the direction of current flow. The low ellipticities may in some cases be associated with the slight off- field propagation. In those cases where this explanation is not applicable perhaps the effects of finite electric fields as studied by *Hu and Fraser* [1992] and *Dowdell et al.* [1993] may be responsible.

Wavelengths vary from 1000 to 6700 km with equal numbers of wave events observed to be travelling earthward as tailward.

Finally, the wave amplitudes observed are typically less than 1 nT, providing energy densities much less than those of the plasma in which they are observed.

From the application of linear Vlasov theory and consistent with *Angelopoulos et al.* [1989], it has been found that the most likely instabilities exciting wave growth are the ion cyclotron anisotropy instability and the kink-like instability both of which may be subject to significant Doppler shifts. Consequently, the properties of these waves in terms of polarization, frequency, wavelength and direction of propagation may vary depending on the form of the observed distribution function. Hence the identification of the instability associated with a particular polarized wave burst is highly sensitive to how accurately the measured distribution function represents that actually present in the plasma over the duration of the wave observation. Because the distribution functions considered here are limited to 2- or 8-min resolution the results presented can only roughly approximate to the true state.

With this limitation in mind, more than 50% of the polarized wave events identified throughout the magnetotail lobes, plasma sheet boundary layer and plasma sheet can be explained in terms of the Vlasov theory of electromagnetic instability without qualification. This study has been based upon the assumption of observation in the source region. In some cases the locations of observation and generation are separated, particularly for those waves identified in the lobes where the plasma energy density is insufficient to support wave growth. If these lobe events are ignored then 70% of the observed polarized wave activity shares the same frequency range and polarization as that predicted by linear Vlasov theory.

Table A1. Normalized Moment Parameters Representative of the Plasma Sheet Boundary Layer with β_c=0.01, and v_A/c=0.005.

Parameter	Core Protons	Parallel Proton Beam	Anti-Parallel Proton Beam	He^+	He^{++}	O^+	e^-
n_j/n_t	0.1	0.3	0.3	0.05	0.05	0.2	1.05
$T_{\perp j}/T_{\|j}$	1.0	8.0	8.0	1.0	1.0	1.0	1.0
$T_{\perp j}/T_{\perp c}$	1.0	50.0	50.0	1.0	10.0	1.0	1.0
v_{0j}/v_A	0.0	0.7	-0.7	0.0	0.0	0.0	0.0

In closing, since the wavelengths of the Pc5 activity (tens of R_E), often observed coincident with the higher frequency ion cyclotron waves, are comparable to the scale size of the near-Earth magnetotail they relate directly to the energy input driving turbulence in the magnetotail. Conversely, the wavelengths of the electromagnetic ion cyclotron wave activity, as presented in Table 1, are typically less than 1 R_E and, as *Bauer et al.* [1995] indicates, such scale sizes correspond to the inertial range in the near-Earth magnetotail environment. Perhaps then the observed Pc3-Pc5 modulation is one manifestation of the redistribution of energy from large-scale macroscopic processes or macroturbulence in the tail to the microscopic scale where velocity space instability may provide microturbulence.

Appendix

Here we show that the influence of heavy ions on wave growth and dispersion in the region of instability may be ignored and demonstrate that the properties of instability remain largely invariant from those at $\mathbf{k}\times\mathbf{B_0}$=0 ($\theta_k$=0°) if θ_k<45°. The validity of these assumptions can be checked by solving the full dispersion relation for parameters representative of the plasma sheet boundary layer and plasma sheet as given in Tables A1 and A2. Figure A1 shows the solution for the parameters of Table A1, which represent the plasma sheet boundary layer. When $\mathbf{k}\times\mathbf{B_0}$=0 the coupling that occurs between the individual roots at the resonances of each species (Figure A1a and A1b) due to the Doppler shift and thermal effects (stopband removal) allows wave growth to occur continuously through the O^+ and He^+ resonances. This causes the dispersion of the growing wave to become close to identical to the result where the same dispersion relation has been solved with heavy ion components replaced with H^+ (Figure A1c and A1d). Plotting the dispersion surface contours (Figure A1e) shows that the coupling extends continuously over all wavenumbers where the instability occurs. Regions of weaker coupling or where the coupling breaks down become apparent at more oblique angles and beyond the range of unstable wavenumbers (e.g., $k_{\|}c/\omega_p$=1.5 and $k_{\perp}c/\omega_p$>1.5). Furthermore, it can be seen that there is only a small variation in the frequency and wavenumber of the most strongly growing frequency at angles θ_K<45°.

Similar results are apparent in Figure A2 representing the wave dispersion for the plasma sheet parameters of Table A2. Here the coupling is due to thermal effects alone. The stopband which exists in the cold plasma case between the H^+ branch cutoff and the He^{++} resonance is removed so that growth extends continuously in frequency through the He^{++} resonance (Figure A2a and A2b). The results appear close to those of the equivalent density H^+-e^- plasma illustrated in Figure A2c and A2d albeit with a slightly lower growth rate in the heavy ion case due to the smaller density of the anisotropic H^+ component. The contour plot showing growth at oblique angles (Figure A2e) indicates that the coupling extends smoothly over the unstable region in k space with the real frequency of maximum growth varying little over angles θ_K<45°.

So for the purpose of identifying the instability responsible for the observed wave activity with θ_k<45°, in these predominately hot plasma regimes, the influence of the heavy ion components and variations in wave dispersion with θ_k may, we believe, be ignored.

Table A2. Normalized Moment Parameters Representative of the Plasma Sheet with β_p=4.0, and v_A/c=0.002.

Parameter	Protons	He^+	He^{++}	O^+	e^-
n_j/n_t	0.88	0.01	0.01	0.1	1.01
$T_{\perp j}/T_{\|j}$	2.5	1.0	1.0	1.0	1.0
$T_{\perp j}/T_{\perp c}$	1.0	0.002	0.02	0.002	0.1
v_{0j}/v_A	0.0	0.0	0.0	0.0	0.0

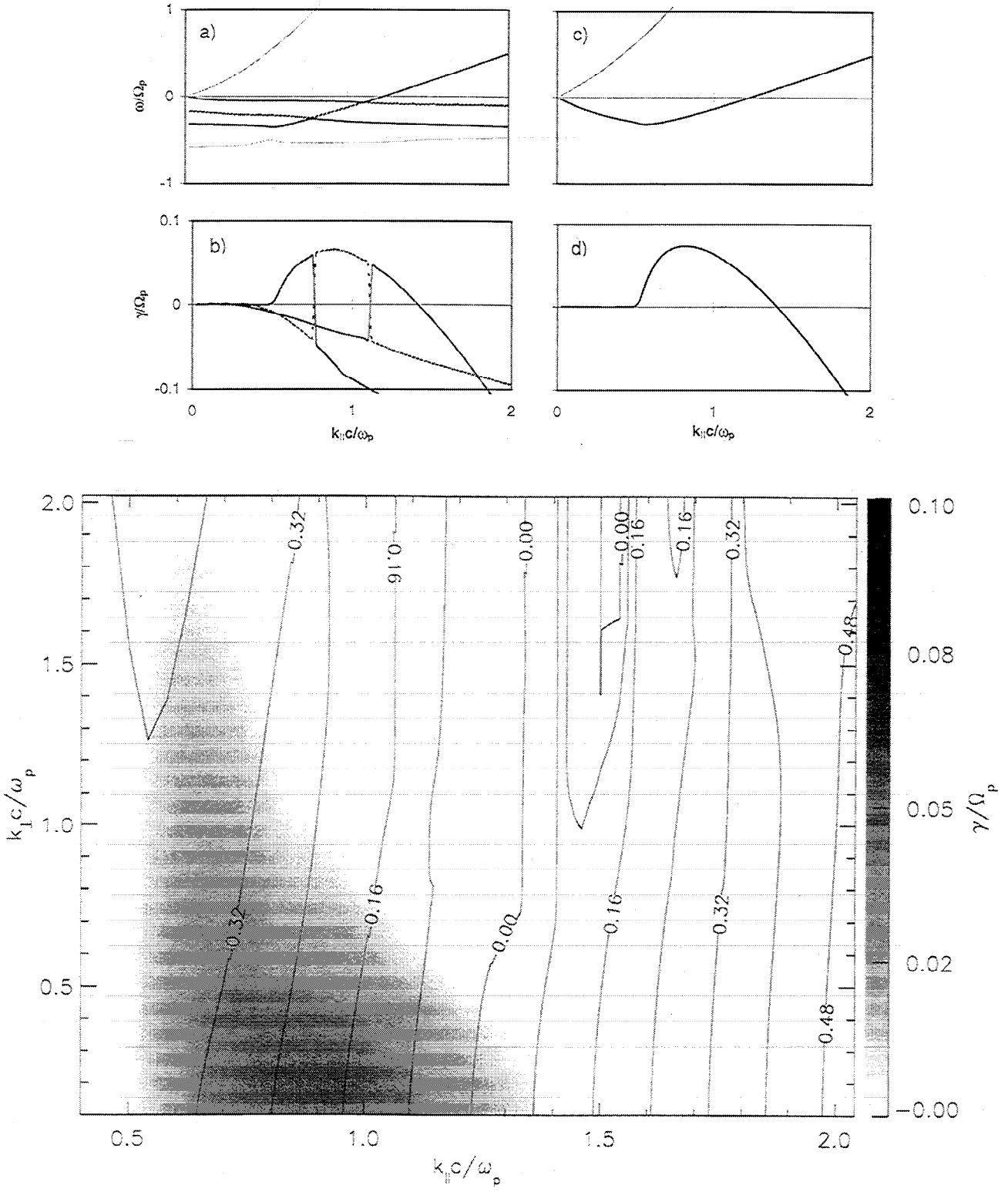

Figure A1. (a, b) The real and imaginary parts of the solution of the linear dispersion relation, equation (1), with $\mathbf{k} \times \mathbf{B}_o = 0$ and $|\omega| < \Omega_p$ for the parameters of Table A1. Each root is presented using the same style line in real frequency (ω/Ω_p) and growth rate (γ/Ω_p). (c, d) The solutions for the equivalent H^+-e^- plasma and (e) the more general solution for oblique propagation again using the parameters of Table A1. In Figure A1e the contours are real frequencies normalized by Ω_p and the greyscale is the temporal growth rate normalized in the same way.

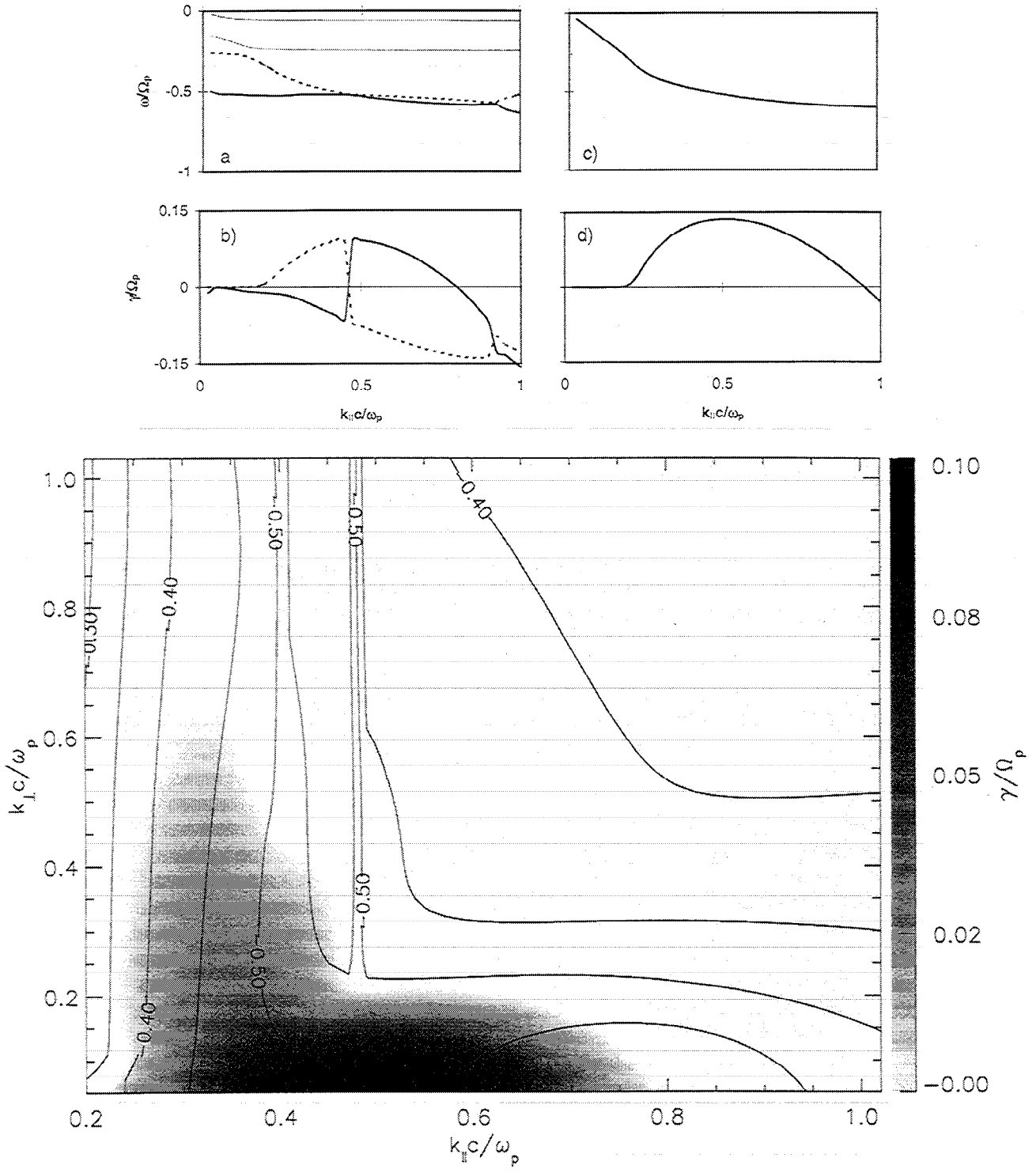

Figure A2. (a, b) The real and imaginary parts of the solutions of the linear dispersion relation, equation (1), with $\mathbf{k} \times \mathbf{B}_0 = 0$ and $|\omega| < \Omega_p$ for the parameters of Table A2. Each root is presented using the same style line in real frequency (ω/Ω_p) and growth rate (γ/Ω_p). (c, d) The solutions for the equivalent H^+-e^- plasma and (e) the more general solution for oblique propagation again using the parameters of Table A2. In Figure A2e the contours are real frequencies normalized by Ω_p, and the greyscale is the growth rate normalized in the same way.

Acknowledgments. The authors would like to thank C. T. Russell, C. Y. Huang and R. C. Elphic for supplying the ISEE data used in this study. In addition the authors extend their gratitude to M. Temerin for his suggestions on improving the manuscript. This research was supported by grants from the Australian Research Council, The University of Newcastle, and NASA (NAG5-3596).

Michel Blanc thanks two referees for their assistance in evaluating this paper.

References

Akimoto, K., and N. Omidi, The generation of broadband electrostatic noise by an ion beam in the magnetotail, *Geophys. Res. Lett., 13*, 97, 1986.

Anderson, B. J., R. E. Denton, and S. A. Fuselier, On determining the polarization characteristics of ion cyclotron wave magnetic field fluctuations, *J. Geophys. Res., 101*, 13195, 1996.

Angelopoulos, V., R. C. Elphic, S. P. Gary, and C. Y. Huang, Electromagnetic instabilities in the plasma sheet boundary layer, *J. Geophys. Res., 94*, 15373, 1989.

Bame, S. J., J. R. Asbridge, H. E. Felthauser, J. P. Glore, G. Paschmann, P. Hemmerich, K. Lehmann and H. Rosenbauer, ISEE-1 and ISEE-2 fast plasma experiment and the ISEE-1 solar wind experiment, *IEEE Trans. Geosc. Elec., GE-16*, 216, 1978.

Barfield, J. N., and P. J. Coleman Jr., Storm related wave phenomena observed at synchronous equatorial orbit, *J. Geophys. Res., 75*, 1943, 1970.

Bauer, T. M., W. Baumjohann, R. A. Treumann, N. Sckopke, and H. Luhr, Low frequency waves in the near-Earth plasma sheet, *J. Geophys. Res., 100*, 9605, 1995.

Burinskaya, T., D. Schriver, and M. Ashour Abdalla, Propagation of whistler waves driven by fine structured ion beams in the magnetotail, *J. Geophys. Res., 99*, 8647, 1994.

Cattell, C. A., F. S. Mozer, R. R. Anderson, E. W. Hones Jr., and R. D. Sharp, ISEE observations of the plasma sheet boundary, plasma sheet and neutral sheet, 2, Waves, *J. Geophys. Res., 91*, 5681, 1986.

Chaston, C. C., Y. D. Hu, B. J. Fraser, R. C. Elphic, and C. Y. Huang, Electromagnetic ion cyclotron waves observed in the near earth plasma sheet boundary layer, *J. Geomagn. Geoelectr., 46*, 987, 1994.

Chaston, C. C., Y. D. Hu, and B. J Fraser, Non-Maxwellian particle distributions and electromagnetic ion cyclotron instabilities in the near-Earth magnetotail, *Geophys. Res. Lett., 24*, 2913, 1997.

Christon, S. P., D. J. Williams, D. G. Mitchell, C. Y. Huang, and L. A. Frank, Spectral characteristics of plasma sheet ion and electron populations during disturbed geomagnetic conditions, *J. Geophys. Res., 96*, 1, 1991.

Coroniti, F. V., and C. F. Kennel, Electron precipitation pulsations, *J. Geophys. Res., 75*, 1279, 1970.

Cuperman, S., Electromagnetic kinetic instabilities in multicomponent space plasmas: Theoretical predictions and computer simulation experiments, *Rev. Geophys., 19*, 307, 1981.

DeCoster, R. J., and L. A. Frank, Observations pertaining to the dynamics of the plasma sheet, *J. Geophys. Res., 84*, 5099, 1979.

Davidson, R. C., and J. M. Ogden, Electromagnetic ion cyclotron instability driven by energy anisotropy in high-beta plasmas, *Phys. Fluids, 18*, 1045, 1975.

Dowdell, G.G, Y. D. Hu, and B. J. Fraser, Linearly polarised electromagnetic ion cyclotron waves in a static background electric field, paper presented at Second South Pacific STEP Workshop, Newcastle, 1993.

Dowdell, G. G., Y. D. Hu, and B. J. Fraser, Linearly polarised electromagnetic ion cyclotron waves in the middle magnetosphere, paper presented at XXI General Assembly of IUGG, Boulder Colorado, July 2-14, 1995.

Eastman, T. E., L. A. Frank, W. K. Peterson, and W. Lennartsson, The plasma sheet boundary layer, *J. Geophys. Res., 89*, 1553, 1984.

Elphic, R. C., and S. P. Gary, ISEE observations of low frequency waves and ion distribution function evolution in the plasma sheet boundary layer, *Geophys. Res. Lett., 17*, 2023, 1990.

Frank, L. A., D. M. Yeager, H. D. Owens, K. L. Ackerson, and M. R. English, Quadrispherical LEPEDEAS for ISEE's -1 and -2 plasma measurements, *IEEE Trans. Geosci. Electr., GE-16*, 221, 1978.

Fraser, B. J., J. C. Samson, Y. D. Hu, R. L. McPherron and C. T. Russell, Electromagnetic ion cyclotron waves observed near the oxygen cyclotron frequency by ISEE 1 and 2, *J. Geophys. Res., 97*, 3063, 1992.

Freund, H. P., and C. S. Wu, Stability of a spherical shell distribution of pickup ions, *J. Geophys. Res., 93*, 14277, 1988.

Fried, B. D., and S. D. Conte, *The Plasma Dispersion Function*, Academic, San Diego, Calif., 1961.

Gary, S. P., and D. Schriver, The electromagnetic ion cyclotron beam anisotropy instability, *Planet. Space Sci., 35*, 51, 1987.

Gary, S. P., and R. Sinha, Electromagnetic waves and instabilities from cometary ion velocity shell distributions, *J. Geophys. Res., 94*, 9131, 1989.

Gary, S. P., and D. Winske, Computer simulations of electromagnetic instabilities in the plasma sheet boundary layer, *J. Geophys. Res., 95*, 8085, 1990.

Gary, S. P., R. A. Gerwin, and D. W. Forslund, Electromagnetic current instabilities, *Phys. Fluids., 19*, 579, 1976.

Gary, S.P., P. D. Convery, R. E. Denton, S. A. Fuselier, and B. J. Anderson, Proton and helium cyclotron anisotropy instability thresholds in the magnetosheath, *J. Geophys. Res., 99*, 5915, 1994.

Hu, Y. D., and B. J. Fraser, Dispersion relation of electromagnetic ion cyclotron waves in a multicomponent plasma with static electric and magnetic fields, *Anare Res. Notes, 88*, 63, 1992.

Hasegawa, A., *Plasma Instabilities and Nonlinear Effects. Physics and Chemistry in Space 8*, Springer-Verlag, New York, 1975.

Kennel, C. F., and H. E. Petschek, Limit on stably trapped particle fluxes, *J. Geophys. Res., 71*, 1, 1966.

Kuznetsova, M. M., and B. Nikutowski, A modified lower hybrid drift instability as a possible mechanism for the generation of magnetic noise bursts in the magnetotail neutral sheet, *J. Geophys. Res., 99*, 4105, 1994.

Lui, A. T. Y., P. H. Yoon, and C.-L. Chang, Quasi-linear analysis of ion Weibel instability in the Earth's neutral sheet, *J. Geophys. Res., 98*, 153, 1993.

Mace, R. L., and M. A. Hellberg, A dispersion function for plasmas containing superthermal particles, *Phys. Plasmas, 2*, 2098, 1995.

Means, J. D., Use of the three-dimensional covariance matrix in analysing the polarisation parameters of lane waves, *J. Geophys. Res., 77*, 5551, 1972.

Rauch, J. L., and A. Roux, Ray tracing of ULF waves in a multicomponent magnetospheric plasma: Consequences for the generation mechanism of ion cyclotron waves, *J. Geophys. Res., 87*, 8191, 1982.

Russell, C. T., The ISEE-1 and ISEE-2 fluxgate magnetometers, *IEEE Trans. Geosci. Electron., GE-16*, 239, 1978.

Russell, C. T., and R. L. Mc Pherron, The magnetotail and substorms, *Space Sci. Rev., 11*, 111, 1972.

Samson, J. C., and J. V. Olson, Data-adaptive polarisation filters for multichannel geophysical data, *Geophysics, 46*, 1423, 1981.

Schriver, R. D., and M. Ashour Abdalla, Generation of high frequency broadband electrostatic noise: The role of cold electrons, *J. Geophys. Res., 92*, 5807, 1987.

Summers, D., and R. M. Thorne, A new tool for analyzing microinstabilities in space plasmas modeled by a generalised Lorentzian (Kappa) distribution, *J. Geophys. Res., 97*, 16827, 1992.

Zhang, Y. L., H. Matsumoto, and Y. Omura, Linear and nonlinear interactions of an electron beam with oblique whistler and electrostatic waves in the magnetosphere, *J. Geophys. Res., 98*, 21353, 1993.

C. C. Chaston, Space Sciences Laboratory, University of California, Berkeley, CA 94720. (ccc@ssl.berkeley.edu)

Y. D. Hu and B. J. Fraser, Department of Physics, University of Newcastle, Callaghan, N.S.W. 2308, Australia.

(Received March 5, 1998; revised September 10, 1998; accepted October 5, 1998.)